



**The Scientific Institute for Advanced Training and Studies**

**Experimental  
and  
Theoretical NANOTECHNOLOGY**

**Vol. 1, No. 3, 2017**

**Yarub Al-Douri  
Editor-in-Chief**

**e-ISSN: 2590-4132**

**Honorary Editor: M. Nayfeh (USA)**

---

**Editors**

S. Abdullah (Malaysia)	H. Ekinici (Turkey)	M-B Leptit (France)	T. E. Simos (Greece)
O. Alani (UK)	S. El-Safty (Japan)	J. Lui (USA)	J. Sing (Australia)
M. Ameri (Algeria)		R. Nowak (Finland)	P. R. Somani (India)
N. E. Arif (Iraq)	Y. P. Feng (Singapore)	S. Radiman (Malaysia)	M. Tanemura (Japan)
V. K. Arora (USA)	L. Feo (Italy)	M. V. Reddy (Singapore)	N. Tit (UAE)
M. Al-Jassim (USA)	M. Henni (UK)	A. H. Reshak (Czech Republic)	K. D. Verma (India)
S. Baroni (Italy)	A.Hui (USA)	A. Rubio (Spain)	S. Wang (Singapore)
M. Bounoudina (Bahrain)	M. R. Johan (Malaysia)	M. Rusop (Malaysia)	J. Whitaker (USA)
Z. Cai (USA)	R. Jose (Malaysia)	P. Ruterana (France)	A.Zaoui (France)
A.Chaudhry (India)	N. Joshi (USA)	P. Schwerdtfeger (New Zealand)	D. H. Zhang (Singapore)
N. E. Christensen (Denmark)	A. H. Jumaa (Iraq)	U.Schwingenschlo egl (Germany)	
D. Chua (Singapore)	M. A. R. Khan (USA)		
	R. Khenata (Algeria)		

---

**Contact us**

Experimental and Theoretical NANOTECHNOLOGY

Prof. Dr. Yarub Al-Douri; Founding Editor-in-Chief :[editor.etn@siats.co.uk](mailto:editor.etn@siats.co.uk)

<http://etn.siats.co.uk>



*Experimental and Theoretical NANOTECHNOLOGY*

**VOL. 1, NO. 3, 2017**

**e-ISSN 2590-4132**

*2017*

## ***Experimental and Theoretical NANOTECHNOLOGY***

Experimental and Theoretical NANOTECHNOLOGY is a multidisciplinary peer-reviewed international journal published four issues a year. It includes specialized research papers, short communications, reviews and selected conference papers in special issues on the characterization, synthesis, processing, structure and properties of different principles and applications of NANOTECHNOLOGY; with focus on advantageous achievements and applications for the specialists in engineering, chemistry, physics and materials science.

Experimental and Theoretical NANOTECHNOLOGY covers and publishes all aspects of fundamental and applied researches of experimental and theoretical nanoscale technology dealing with materials synthesis, processing, nanofabrication, NANO probes, spectroscopy, properties, biological systems, nanostructures, NANO electronics, Nanooptics, NANO-mechanics, NANO-devices, NANO biotechnology, nanomedicine, Nano toxicology within the scope of the journal. Experimental and Theoretical NANOTECHNOLOGY aims to acquire the recent and outstanding researches for the benefit of the human being.

## Comparative Study of attenuation properties of some ternary borate glass systems

R. S. Kaundal<sup>1,\*</sup>, Z. I. Takai<sup>1</sup>

<sup>1</sup>Department of Physics, School of Physical Sciences, Lovely Professional University, Phagwara, Punjab-144411, India.

\*E-mail: rajinder.17099@lpu.co.in

Received 19 march. 2016; Revised 22 march 2016; Accepted 1 May 2017

Some borate based systems doped with sodium, zinc and lead are chosen to study gamma ray mass attenuation properties. Different parameters like mass attenuation, half value layer and mean free path have been analyzed at different photon energies. The values of molar volume have been estimated from density values to get idea regarding the compactness of the network structure. XCOM computer software has been employed to estimate mass attenuation coefficient at various energies. Further the values of HVL for the studied systems are compared with standard radiation shielding materials like concrete.

**Keywords:** Glasses, Density, Shielding, Mean free path, Half value layer

**PACS:** 81.05.Kf, 65.40.De, 28.41.Qb, 72.15.Lh, 87.57.Q-

### 1. Introduction

Now days, the use of nuclear energy and radiation is necessary in modern society such as nuclear power plants and radiotherapy. Handling radiation sources with safe is essential. The knowledge of gamma-ray interaction parameters such as mass attenuation coefficient, effective atomic number, electron density, total interaction cross-section, half value layer, mean free path, etc. is very important in the designing of radiation shielding materials.[1]

It is worth mentioning that, radioactive sources are hazard to environment and the intensity of radioactive materials varies in proportionality to the factors like time, distance and nature of shielding material. The glasses containing heavy metals are the promising candidates in the field of radiation shielding materials. Samir et.al [2] have studied experimentally the attenuation properties of lead zinc borate glasses at energies at 662 KeV, 1173 KeV, 1332 KeV and 2641 KeV by using Co-60. In his findings the authors have concluded that addition of heavy metal like PbO helps in improving the shielding properties of the glasses. Generally borate ( $B_2O_3$ ) and silicates ( $SiO_2$ ) are used as the glass formers.  $SiO_2$  window glass silica finds many applications and is also used as reflector in electrical appliances.[3] These borate and silicate glasses when doped with heavy metals find applications in radiation shielding materials.[4-5]

V.P.Singh et. al [6] have studied the systems lead bismuth borate, lead borate and bismuth borate for gamma ray exposure build up factors. Again improved shielding properties of these materials were concluded by the authors H.Singh et al [7] in the study of radiation

shielding properties of lead borate and zinc glasses. Further it was concluded by many authors that increasing the content of PbO in glasses improve its hardness. It was observed by many authors [7] that the glasses containing heavy-metal oxide like barium, lead and bismuth can be used as alternate to conventional shielding materials due to their high effective atomic number and strong absorption coefficient. [8] However one of the most important type of radiation for which shielding is needed in a nuclear reactor are initially neutron and gamma-ray coming-out from the core and then gamma-ray produced by neutron interaction with the material external to the reactor core [9-10]. Therefore any type of material can be used for radiation shielding once it has capability to absorb the incident radiation to a certain level. In the area shielding material and propose same research works with different glass as new shielding material [11].

In the light of above discussion the author in the present paper has shown interest in the borate glass system containing oxides of boron, zinc and lead. The density and molar volume values were used to get the idea regarding rigidity of the network structure. Mass attenuation coefficient of the glass systems have been studied in the energy range from 1KeV to 100 GeV. Further the values of mean free path and half value layer are estimated and analyzed.

## 2. Computational Technique

### (I) Linear attenuation coefficients

The mass attenuation coefficients of the selected heavy metal oxide glasses were calculated using the formula as given below

$$\mu_m = \sum_i^n w_i(\mu/\rho) \tag{1}$$

Where  $w_i$  is the weight and  $\mu/\rho$  is the mass attenuation coefficient of the sample. The  $\mu/\rho$  values can be taken from XCOM program or user-friendly Win Xcom software. The linear attenuation coefficient (in  $\text{cm}^{-1}$ ) is multiplication of  $\mu/\rho$  value and density of the glass.

### (II) Mean Free Path and Half Value Layer

The mean free path (MFP) is reciprocal of linear attenuation coefficient. Mean free path (MFP) and half valve layer (HVL) can be found using the following relations

$$\text{MFP } (\lambda) = 1/\mu \tag{2}$$

$$\text{HVL} = 0.693/ \mu \tag{3}$$

The molar volume  $V_g$  was evaluated using the relation

$$V_g = M/\rho \tag{4}$$

Here  $\rho$  is the density and  $M$  is the molar mass

The Computational Technique has proven to be one of the most accurate methods for the computation of the electronic structure of solids [12-15].

## 3. Results and discussion

The chemical composition, molar volume and density of samples S1, S2 and S3 have been taken from literature [2,16-17] are listed in the Table 1. The density increases with increase in heavy metal in the glass system. The density values are helpful in estimating the molar volume of glass samples given in Table 1. The molar volume, which gives idea as the



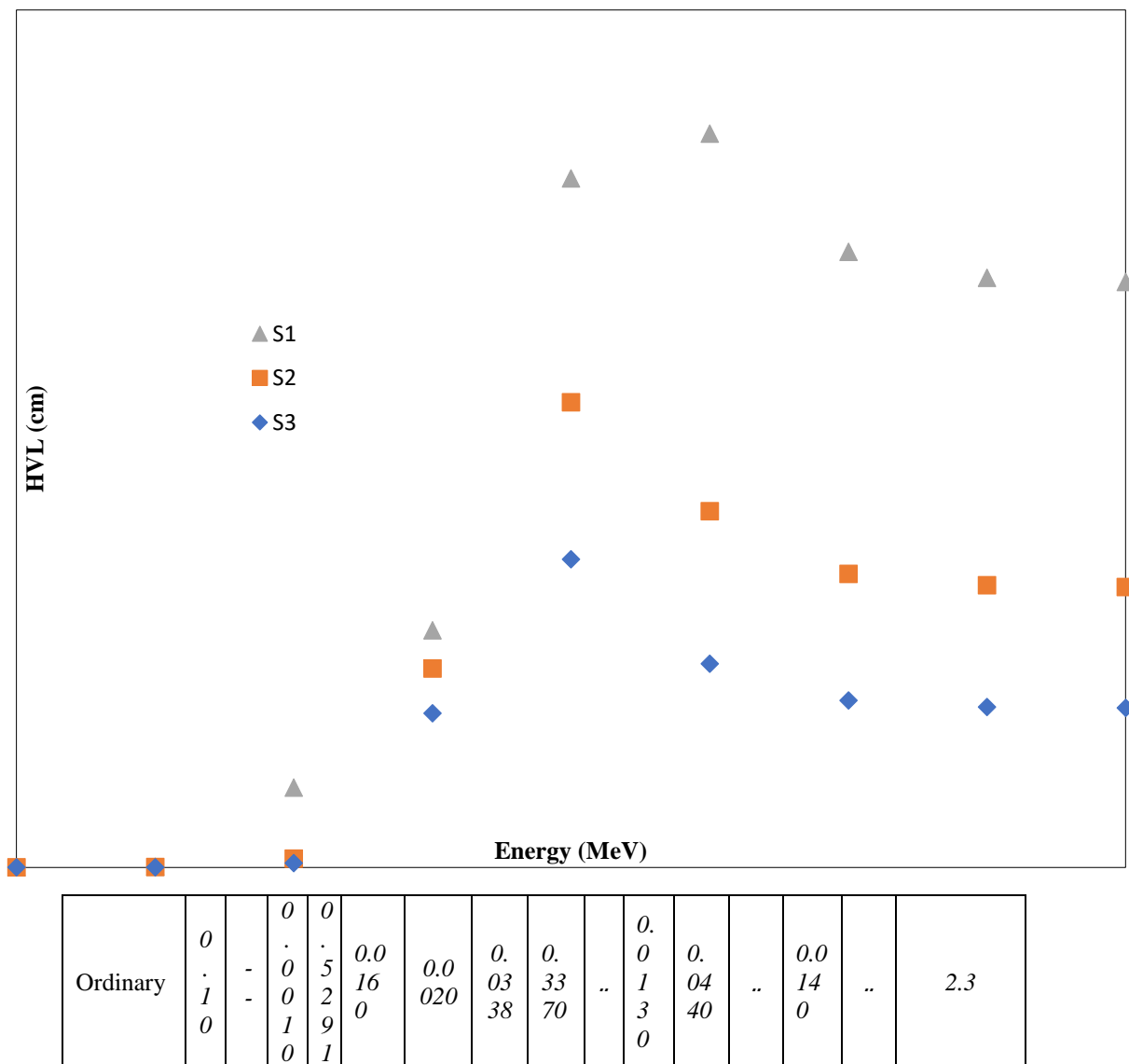


Figure 1: Plot of HVL for various samples as a function of photon energy.

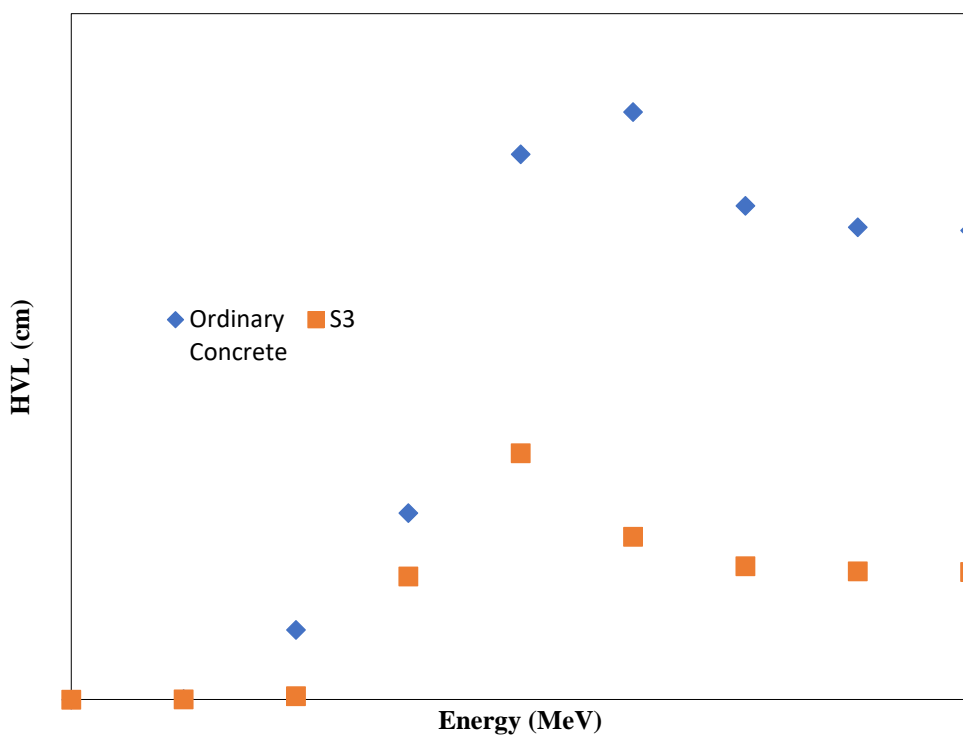


Figure 2 Plot of HVL for sample S3 and ordinary concrete as a function of photon energy.

The values of mean free path are listed in table 4 for the studied samples.

Table 4 : Theoretical result of mean free path

Energy	Mean Free Path		
	S1	S2	S3
1.00E-03	0.00013	9.32E-05	6.57E-05
1.00E-02	0.014295	0.00929	0.003849
1.00E-01	2.143476	0.231118	0.114632
1.00E+00	6.385411	5.357793	4.14733
1.00E+01	18.54795	12.52097	8.292135
1.00E+02	19.75297	9.591866	5.484693
1.00E+03	16.57262	7.905263	4.490434
1.00E+04	15.87377	7.595321	4.317534
1.00E+05	15.7598	7.547113	4.291693

## 5. Conclusion

It can be concluded from the result that in all the studied glass systems S3 has minimum HVL value and low mean free path. In light of this analysis shown that the glass S3 is suitable for radiation shielding because of high mass attenuation and low HVL value.

## References

- [1] C Bootjomchai, J. Laopaiboon, C.Yenchai, R.Laopaiboon. Radiation Physics and Chemistry **81(7)** (2012) 785.
- [2] AN. Kannappan, S. Thirumaran, R. Palani, ARPN Journal of Engineering and Applied Sciences **4(1)** (2009) 27.
- [3] N. A.A.Al-Tememe, K.J. Al-Ani Salwan, Y.S. Al-M. Dhefah, Int. J. Nanoelectronics and Materials **6** (2013) 9.
- [4] A. L. Conner, H. F. Atwater, E. H. Plassmann, J. H. McCrary, Physical Review A, **1**, (1970), 539.
- [5] E.R Atta, Kh.M Zakaria, A.M Madbouly, International Journal of Recent Scientific Research, **6(5)** (2015) 4263.
- [6] V.P Singh, N.M.Badiger, J.Kaewkhao, Journal of Non-Crystalline Solids, **404** (2014)167.
- [7] H. Singh, K. Singh, L. Gerward, K.Singh, H. S. Sahota and R. Nathuram, Nuclear Instruments and Methods in Physics Research B **207** (2003) 257.
- [8] N. Singh, K. J. Singh, K. Singh and H. Singh, Nuclear Instruments and Methods in Physics Research Section B: Beam Interactions with Materials and Atoms **225(3)** (2004) 305.
- [9] A.Khanna, S.S.Bhatti, K.J.Singh, K.S.Thind, Nuclear Instruments and Methods in Physics Research Section B: Beam Interactions with Materials and Atoms **114(3)** (1996) 217.
- [10] N.S.Hussain, M.A.Lopes and J.D. Santos, Materials Chemistry and Physics **88(1)** 2004 5.
- [11] A.G.Mostafa, H.A Saudi, M.Y. Hassan, S.M Salem, S.S Mohammad, American Journal of Modern Physics **4(4)** (2015)149.
- [12] A.H. Reshak, O.V. Parasyuk, A.O. Fedorchuk, H. Kamarudin, S. Auluck and J. Chysky, J. Phys. Chem. B, **117(48)** (2013) 15220.
- [13] A.H. Reshak, Xuean Chen, S. Auluck, H. Kamarudin, Jan Chysky, A. Wojciechowski and I.V. Kityk, J. Phys. Chem. B, **117(45)** (2013) 14141.
- [14] A.H. Reshak, H. Kamarudin, I.V. Kityk and S. Auluck, J. Phys. Chem. B, **116(45)** (2012) 13338.
- [15] A.H. Reshak, H. Kamarudin and S. Auluck, J. Phys. Chem. B, **116(15)** (2012) 4677.
- [16] P.Limkitjaroenporn, W. Chewpraditkul, J. Kaewkhao, S.Tusharoen, Energy Research Journal **2(1)**, (2011) 29.
- [17] S.Y El-Kameesy, S.A El-Ghany, M.A.E-H.Azooz, Y.A.A.El-Gammam, World Journal of condensed matter Physics, **3** (2013) 198.

## Modelling of Silicon Based Electrostatic Energy Harvester for Cardiac Implants

Suhaib Ahmed<sup>1,\*</sup>, Sakshi Koul<sup>2</sup>, Vipin Kakkar<sup>3</sup>

<sup>1,3</sup>Department of Electronics and Communication Engineering, Shri Mata Vaishno Devi University, Katra, J&K - 182 320, India.

<sup>2</sup> Department of Electronics and Communication Engineering, National Institute of Technology, Srinagar, Hazratbal, J&K – 190 006, India.

\*) E-mail: sabatt@outlook.com

Received 19 march. 2016; Revised 22 march 2016; Accepted 1 May 2017

The concept of Energy Harvesting using the ability of heart to develop an acceptable amount of power for its natural operation (up to 10W) could address the power source requirements of leadless pacemakers. This paper presents a new structural geometry of Silicon based Electrostatic Energy Harvester which uses angled electrodes unlike the traditional harvesters for these pacemakers. It is observed that this topology provides a greater change of capacitance with respect to displacement compared to conventional topologies as it combines both In-Plane Gap and In-Plane Area Overlap capacitances. This harvester can thus be used as an alternate to the conventional battery sources used and act as a constant voltage source for various components of the pacemaker.

**Keywords:** Energy harvesting, biomechanics, electrostatic, electrode, pacemaker

**PACS:** 84.32.Tt, 87.80.-y, 87.85.G-, 87.85.Qr, 87.85.Tu

### 1. Introduction

The output mechanical energy of the heart is in the order of ~1W. As the overall efficiency of the heart is about 20- 25%, this corresponds to an overall energy consumption of several Watts [1]. Therefore, it might be possible to scavenge tens of microwatts from the heartbeat by an energy harvester without affecting the natural functioning of the heart [2]. Hence, the goal of achieving self-powered electronic devices or battery less devices has gained attention and a lot of efforts have been initiated in this field. Energy harvesting is thus available as an option in powering of large number of devices and systems including the medical implants. Pacemaker is one such active implant device that needs continuous supply of power because the heart has to generate pulses all the time. Furthermore, knowing the fact that a significant amount of energy is produced in the human body, it motivates the development of an element or system that could extract a part of it. This generated energy is available at various locations in the body and can take different forms such as dissipated heat, inertia, muscle contraction, joint movement, heel strike, etc.

Vibrations are an effective source of energy present in the human body and we can use these vibrations for harvesting energy by converting the vibrations to electrical power. This idea of harvesting electrical energy from the body vibrations such as heartbeats, is gaining commendable interdisciplinary research interest. An analysis and comparison of three different types of vibration energy harvesting techniques: Electrostatic; Piezoelectric and, Electromagnetic Energy Harvesting for pacemakers has been presented in [3]. It can be concluded from the survey that Electrostatic based Transduction method of energy harvesting is most suitable for cardiac implants. The advantage of this technique is that it can be easily realizable as MEMS. Moreover, the output levels obtained satisfy the power requirements. One such research has been presented in [4] wherein a capacitance detection based biosensor has been proposed which is Electrostatic in nature. The most essential feature of implants is that they should have small size that can be satisfied by using Electrostatic Transducer structure.

## 2. Standard Topologies of Electrostatic Transduction

The electrostatic transduction mechanism uses a variable capacitor whose capacitance is changed as a function of the mechanical displacement denoted by  $x$ . In order to achieve maximum amount of harvested energy, the capacitance variation with respect to displacement needs to be as large as possible. There are various topologies for the MEMS electrostatic devices that differ in actuation direction. These standard topologies of the electrostatic transducers [5-7] and their capacitances are discussed below:

### 2.1 In-Plane Overlap

It is basically an inter-digitated comb structure with variable overlap of fingers and movement in plane as shown in Fig 1. This develops a capacitance variation by vibrating in plane of the device. For limiting the minimum dielectric gap in the inter-digitated fingers, the mechanical stops can be used.

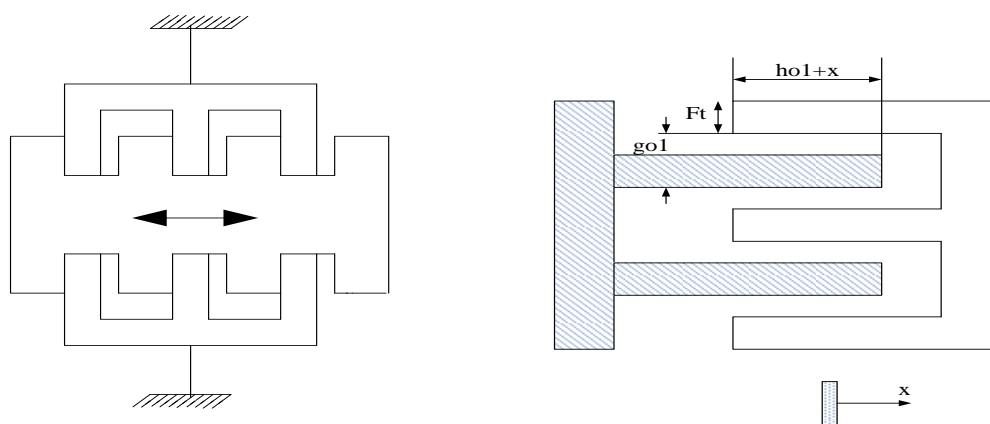


**Figure.1:** (a) In-Plane Overlap Converter (b) In-Plane Overlap Comb structure

Here  $g_{o1}$  is the initial gap between fingers,  $h_{o1}$  is the initial overlap of the fingers,  $F_t$  is the height of the electrode elements,  $x$  is the displacement, and  $\epsilon$  is the permittivity of the dielectric material between the electrodes of the capacitor. The capacitances  $C_1$  and  $C_2$  change with the movement of the mobile part of the structure. As can be seen,  $C_1$  and  $C_2$  appear to be in parallel hence are added up, i.e.  $C = C_1 + C_2$  where,  $C = 2C_1 = 2C_2$ .

We know,

$$\text{Capactiance} = \epsilon \frac{\text{Area of electrodes}}{\text{distance between electrodes}} \tag{1}$$

Here,

$$\text{Area of the electrode} = F_t [h_{o1} + x] \tag{2}$$

Hence, capacitance variation obtained can be given by the relation,

$$C = \frac{2\epsilon F_t [h_{o1} + x]}{g_{o1}} \tag{3}$$

### 2.2 In-Plane Gap Closing

This represents an inter-digited comb structure with variable gap between fingers and movement in plane as shown in Fig. 2.

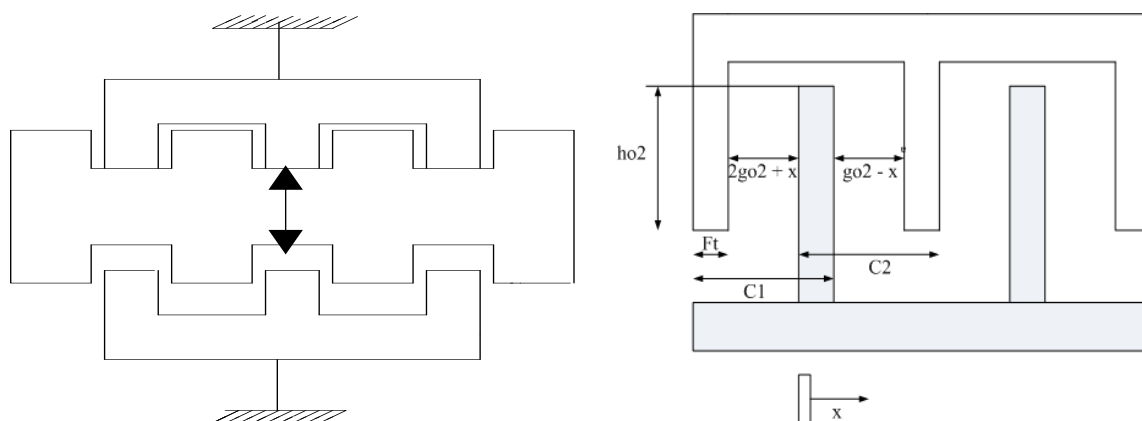


**Figure. 2 :** (a) In-Plane Gap Closing Converter (b) In-Plane Gap Closing Comb structure

Here  $g_{o2}$  is the initial gap between the fingers,  $h_{o2}$  is the initial overlap of the fingers and  $S_{o2}$  is the minimum gap at  $x_0$ . Since the two capacitances  $C_1$  and  $C_2$  appear to be in parallel combination, so applying the rule for total capacitance of two capacitances in parallel we get:

$$C = C_1 + C_2 \tag{4}$$

where,

$$C_1 = \frac{\epsilon F_t h_{o2}}{2g_{o2} + x} \text{ and } C_2 = \frac{\epsilon F_t h_{o2}}{g_{o2} - x} \tag{5}$$

and,

$$g_{o2} = x_o + S_{o2} \tag{6}$$

Substituting these values, we get

$$C = \epsilon F_t h_{o2} \left[ \frac{1}{2g_{o2} + x} + \frac{1}{g_{o2} - x} \right] \tag{7}$$

Simplifying it further, we get the final capacitance as,

$$C = \frac{\epsilon F_t h_{o2} [3(x_o + S_{o2})]}{(x_o + S_{o2} - x)(2(x_o + S_{o2}) + x)} \tag{8}$$

### 2.3 Out-of-Plane Gap Closing

This topology shown in Fig. 3 represents a planar structure with variable air gaps between plates and perpendicular motion to the plane. The capacitance variation is obtained here by varying the gap between the fingers.

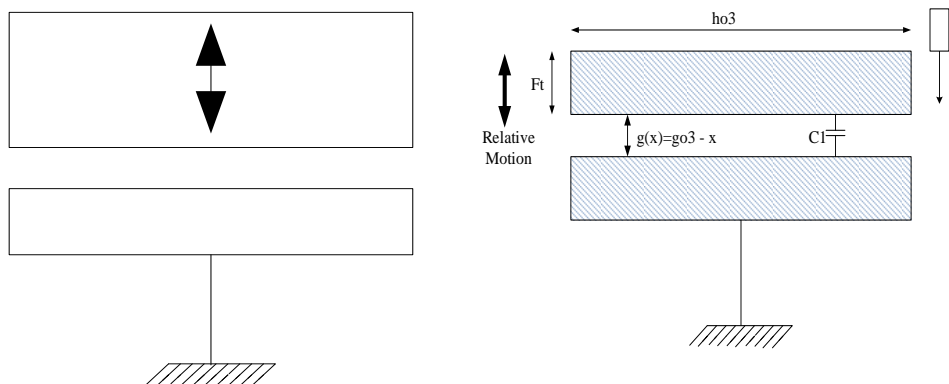


**Figure. 3 :** (a) Out-of-Plane Gap Closing Converter (b) Out-of-Plane Gap Closing structure

In this converter type, the motion of the mobile part of the structure is out of plane. The mobile electrode moves above the fixed electrode, this induces a variation of the gap between the electrode and the mobile electrode. If  $g_{o3}$  is the initial gap between the two electrodes and  $h_{o3}$  is the initial overlap of the fingers, then

$$\text{Area of the electrode} = F_t [h_{o3}] \tag{9}$$

$$C = \frac{\epsilon h_{o3} F_t}{(g_{o3} - x)} \tag{10}$$

### 3. Proposed Topology and Implementation

We can categorize the above discussed three standard cases either as Area-Sensitive or as Gap-Sensitive. Area-Sensitive topology includes the In-Plane Overlap topology where as the Gap-Sensitive topology includes the In-Plane Gap Closing and the Out-of-Plane Gap Closing topologies. In the Area-Sensitive topology, the capacitance variation is obtained by variation of area of overlap between the two electrodes of the capacitor structure where as the gap between the electrodes remains constant throughout. In the Gap-Sensitive topology, the capacitance variation is obtained by the change in the gap between the electrodes of the capacitor structure where as the area of overlap of the two capacitor plates or electrodes remains the same. In order to maximize the obtainable capacitance variation, we can think of a more advanced geometry that includes the sensitivity of both area and gap.

A new geometry for the fingers (electrode elements) of the harvester structure which is made of Silicon (Si), in which an angular component 'A' in the electrode geometry introduced, has been proposed in this paper as shown in the Fig 4. By doing so we are able to obtain both the area and gap based capacitance variations.

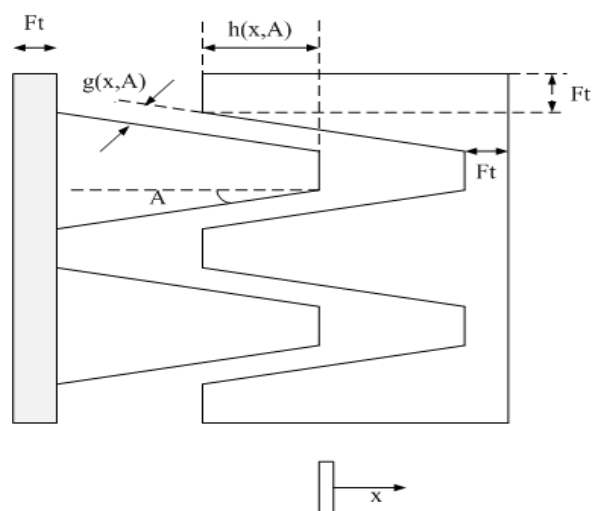


**Figure. 4:** Architecture of the Proposed Comb Structure based Electrostatic Converter

Various design parameters considered in the proposed topology are  $x$  which is the displacement of the mobile part of the inter-digitated comb structure;  $g(x,A)$  the gap between the fingers as a function of angle  $A$  and displacement  $x$ ;  $h(x,A)$  is the overlap between the fingers as a function of angle  $A$  and displacement  $x$ .

### 3.1 Capacitances Calculations

Various dimensions of the proposed structure are shown in Fig. 5. The vibration source causes a displacement of the mobile part of the comb structure that is denoted by  $x$ . Now this displacement  $x$  causes the variation of capacitance by varying the area of overlap of the two electrodes as well as the gap between them.

First of all considering the variations due to the changes in the area of overlap of the two electrodes:

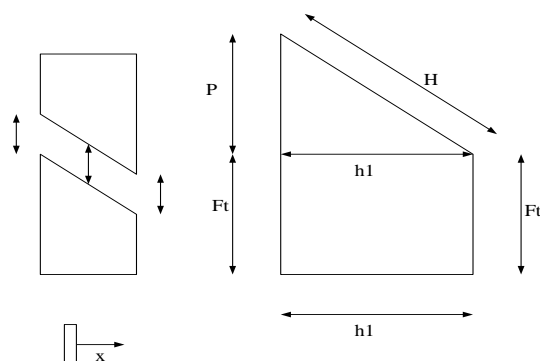


**Figure. 5:** Variations due to the changes in the area of overlap of the two electrodes

$$\text{Area of the overlapping parts of the electrodes} = F_t * H = \left( \frac{h_1}{\cos A} \right) * F_t \tag{11}$$

Where,  $h_1$  is the initial overlap length of the mobile and the fixed part of the structure. Therefore, Capacitance is given by the expression:

$$C_1 = \frac{2\mathcal{E}(h_1 + x/\cos A)F_t}{(g_o - x)} \tag{12}$$

We have to consider the variations caused in the capacitance due to the changes in the gaps between some of the other parts of the two electrodes. The variations of capacitance obtained here are denoted by  $C_2$  and can be represented as in Fig. 6.

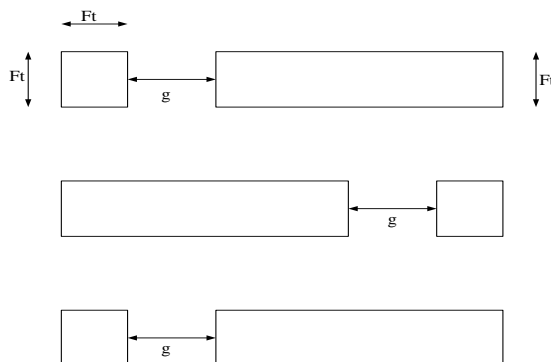


**Figure. 6:** Variations due to the changes in the horizontal gap between the two electrodes.

Here we have

$$g = g_o - x \tag{13}$$

$$\text{Area of the overlapping parts of the electrodes} = F_t * F_t \tag{14}$$

And,

$$C_2 = \frac{3\epsilon(F_t^2)}{(g_o - x)} \tag{15}$$

Next, considering only the changes in the gap between slanting faces of the electrodes as shown in Fig. 7

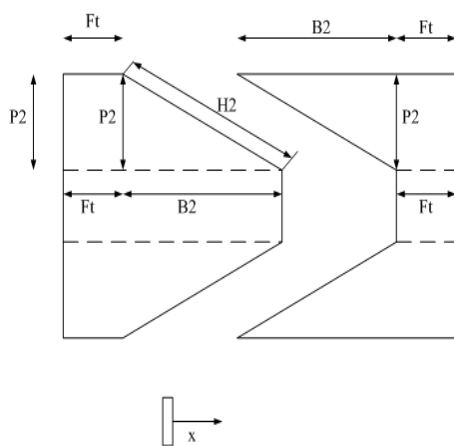


**Figure. 7:** Variations due to the changes in the slanting gap between the two electrodes

$$\text{Area of the overlapping parts of the electrodes} = F_t * H_2 = \left(\frac{B_2}{\cos A}\right) * F_t \tag{16}$$

$$C_3 = \frac{2\epsilon B_2(F_t)}{\cos A (g_o - x)} \tag{17}$$

### 4. Results and Discussion

An energy source for leadless cardiac pacemaker should preferably be a perpetual power supply rather than a traditional battery with limited longevity. In order to achieve the conversion of these mechanical forces into electrical energy, the Electrostatic based transduction has been selected in the proposed design. An electrostatic transducer is basically a capacitor which capacitance is changed by mechanical forces, and from which energy is extracted by appropriate charge-discharge cycles. This method of transduction of energy has wide range of tuning capabilities and a large part of the incoming mechanical energy can be converted into electrical energy. The requirements for this are an efficient design of the transducer and power management circuit. Several topologies of electrostatic based energy harvesters that can be used to satisfy this need have been discussed, modeled and compared with the proposed topology using the SIMULINK package of MATLAB. The simulation parameters are given in Table 1.

Table 1: Design parameters of the proposed energy harvester.

Parameters	Value
Permittivity ( $\epsilon$ )	$11.7 \times 8.854 \times 10^{-12}$ F/m
Angle ( $A$ )	0.203 rad
Height of electrode ( $F_t$ )	50 $\mu\text{m}$
Initial Gap between electrodes ( $g_0$ )	25 $\mu\text{m}$
Initial Overlap of Fingers ( $h_1$ )	20 $\mu\text{m}$

The graph in Fig. 8 shows that the capacitance variation of the proposed topology with respect to displacement is greater as compared to standard topologies and hence a greater extent of energy can be harvested for cardiac implant.

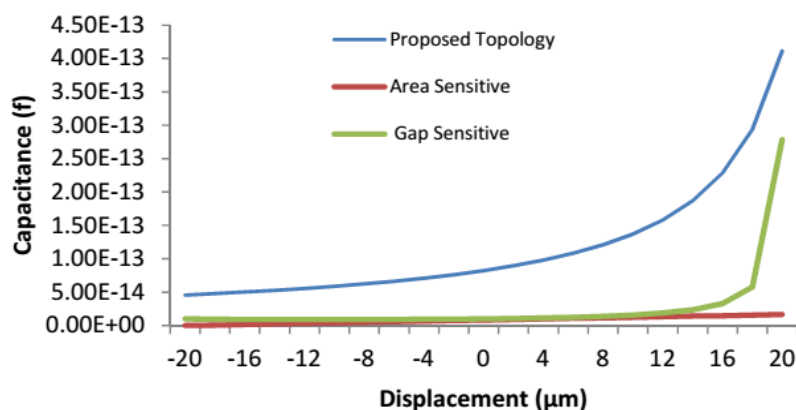


Figure. 8: Variation of Capacitance obtained with respect to Displacement of various topologies

## 5. Conclusion

A new design for the electrode elements of an Electrostatic Energy Harvester is presented. This design is an improvement to the standard topologies of the Electrostatic Energy Harvester. This configuration provides relatively very large capacitance variation with respect to the displacement of the electrode elements of the harvester and is particularly suitable for leadless pacemaker geometric requirements as the dimensions of the electrode elements are in accordance with the leadless cardiac implant requirements.

## References

- [1] N. Westerhof, Cardiac Work and Efficiency, *Cardiovascular Research*, **48** (2000) 4-7.
- [2] M. Deterre, S. Risquez, B. Bouthaud, R. D. Molin, M. Woytasik, E. Lefeuvre, Multilayer Out-of-Plane Overlap Electrostatic Energy Harvesting Structure Actuated by Blood Pressure for Powering Intra-Cardiac Implants, *Journal of Physics: Conference Series*, **476** (2013).
- [3] S. Koul, S. Ahmed, V. Kakkar, A Comparative Analysis of Different Vibration Based Energy Harvesting Techniques for Implantables, Proc. IEEE International Conference on Computing Communication and Automation (ICCCA), India (2015) 979-983.
- [4] V.L.S. Fan, Y. Yusof, Design of Fully Integrated Impedimetric CMOS Biosensor for DNA Detection, *Int. J. Nanoelectronics and Materials*, **8** (2015) 55-60.
- [5] S. Boisseau, G. Despesse, B. A. Seddik, *Small Scale Energy Harvesting*, InTech, France (2012) 91-134.
- [6] S. Boisseau, G. Despesse, T. Ricart, E. Defay, A. Sylvestre, Cantilever-based Electret Energy Harvesters, *Smart Materials and Structure*, **20** (2011).
- [7] C. P. Le, E. Halvorsen, Electrostatic Modeling of In-Plane Overlap Energy Harvesters, *PowerMEMS* (2009) 1-4.

## Numerical investigation of natural convection heat transfer in a cavity utilizing Al<sub>2</sub>O<sub>3</sub>-Water nanofluid: Effect of baffle height

Amin Habibzadeh<sup>1,\*</sup>, Rahman Zeighami<sup>2</sup>

<sup>1</sup> Department of Mechanical Engineering, Payame Noor University, Urmia, Iran

<sup>2</sup> Sama technical and vocational training college, Department of Mechanical Engineering, Islamic Azad University, Urmia branch, Urmia, Iran

\*)Email: amin.habibzadeh@yahoo.com.

Received 19 march. 2016; Revised 22 march 2016; Accepted 1 May 2017

The objective of this work is to investigate numerically the single phase natural convective heat transfer in a cavity with baffle utilizing Al<sub>2</sub>O<sub>3</sub>-water nano fluid. The study is carried out numerically for a range of baffle heights,  $h=0.2, 0.5$  and  $0.8$ . Results are presented in the form of streamline and isotherm plots. The results show that heat transfer decreases considerably with increasing partition height. For the two baffle cavity, as the height of baffle increases, separation in the vortices is seen and there is only conduction heat transfer between two baffles. Compared to the top-attached cavity, for the top-attached cavity, streamlines and isotherms are symmetric to the central line. For the two baffle cavity, all the plots are symmetric to the central line.

**Keywords:** Nanofluid; Natural convection; Cavity.

PACS: 81.07.Nb; 47.55.P-; 42.50.Pq.

### 1. INTRODUCTION

Natural convection in cavities is an example of the confined fluid in many technical applications such as electronic industry, cooling systems for nuclear reactors, heat exchangers, solar energy collectors, transportation, drying technologies, chemical processing equipment and etc. A numerous number of experimental and theoretical studies have been done to investigate the flow in cavities. The term of nanofluid which is introduced by Choi [1], refers to a mixture of solid-liquid that solid nanoparticles are dispersed in a fluid. Although a lot of studies have been carried out to investigate the natural convection in cavities [2-5], most of them have considered cavity without partitions. Anilkumar and Jilani [6] studied heat transfer enhancement of nano fluid in a finned cavity investigated for various pertinent parameters like volume fraction, fin height, Rayleigh numbers and aspect ratio of the cavity. The results showed that the presence of nano particles in the fluid alters the structure of the fluid flow.

Moreover, as Rayleigh number increases, natural convection overcomes and the temperature variation is restricted over a gradually diminishing region around the fin. It is also noticed that the heat affected zone becomes larger with the increasing fin height. Habibzadeh et al. [7] investigated the natural convection heat transfer of a partitioned square cavity filled with Al<sub>2</sub>O<sub>3</sub>-water nanofluid. According to the results, the partition height and Rayleigh number increasing leads to the decrease of the heat transfer rate and increase of the average Nusselt number, respectively. Also it is proved that the average Nusselt number is maximum when the partition is placed at the center. Sayehvand et al. [8] studied the natural convection heat transfer in a partitioned square cavity using computational fluid dynamics. They showed that Rayleigh number and height of the partition are important factors that extremely affect the streamlines and isotherms and for a fixed amount of the partition height, Nusselt number increases as the Rayleigh number goes up. The aim of this study is to study a cavity containing baffle in 3 conditions: baffle attached to the bottom wall, baffle attached to the top wall, 2 baffles attached to the top and bottom walls.

### 2. Physical model and governing equation

Fig. 1 displays the schematic diagram considered in this study which is a two dimensional cavity containing insulated baffles. The horizontal walls of the cavity are assumed to be insulated while the left and right vertical walls are maintained at a uniform temperature ( $T_h$ ) and ( $T_c$ ), respectively as the heated and cooled walls.

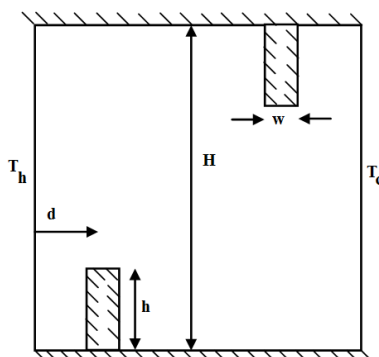


**Figure1.** Schematic diagram of the cavity

The cavity is filled with nanofluid which is composed of Aluminum oxide nano particles in water. The nanofluid is Newtonian, incompressible, and laminar and is assumed to have uniform shape and size. Also, it is assumed that the base fluid and the nanoparticles are in thermal equilibrium and no slip occurs between them. Constant thermophysical properties are considered for the nanofluid, except for the density variation, which is determined based on the Boussinesq approximation.

Table 1. Thermophysical properties of base fluid and nanoparticles.

Property	Water	Al <sub>2</sub> O <sub>3</sub>
$\rho$ (kg/m <sup>3</sup> )	997.1	3970
$C_p$ (J/kgK)	4179	765
$k$ (W/mK)	0.613	40
$\alpha \times 10^7$ (m <sup>2</sup> /s)	1.47	131.7

$\beta_T \times 10^6$ (1/K)	210	24
-----------------------------	-----	----

Under the above assumptions, the steady-state two-dimensional dimensionless government equations are:

$$\frac{\partial U}{\partial X} + \frac{\partial V}{\partial Y} = 0$$

$$U \frac{\partial U}{\partial X} + V \frac{\partial U}{\partial Y} = -\frac{\rho_f}{\rho_{nf}} \frac{\partial P}{\partial X} + \frac{1}{\nu_f \text{Re}} \frac{\mu_{nf}}{\rho_{nf}} \left( \frac{\partial^2 U}{\partial X^2} + \frac{\partial^2 U}{\partial Y^2} \right)$$

$$U \frac{\partial V}{\partial X} + V \frac{\partial V}{\partial Y} = -\frac{\rho_f}{\rho_{nf}} \frac{\partial P}{\partial Y} + \frac{1}{\nu_f \text{Re}} \frac{\mu_{nf}}{\rho_{nf}} \left( \frac{\partial^2 V}{\partial X^2} + \frac{\partial^2 V}{\partial Y^2} \right) + \frac{(\rho\beta)_{nf}}{\beta_f \rho_{nf}} Ri\theta$$

$$U \frac{\partial \theta}{\partial X} + V \frac{\partial \theta}{\partial Y} = -\frac{\alpha_{nf}}{\alpha_f} \frac{1}{\text{PrRe}} \left( \frac{\partial^2 \theta}{\partial X^2} + \frac{\partial^2 \theta}{\partial Y^2} \right)$$

where  $\alpha$  is the thermal diffusivity of the nanofluid that is expressed by :

$$\alpha_{nf} = \frac{k_{eff}}{(\rho c_p)_{nf}}$$

The effective dynamic viscosity of the nanofluid is given by Brinkmann's model:

$$\mu_{nf} = \frac{\mu_f}{(1-\phi)^{2.5}}$$

The effective density of a fluid containing suspended particles is given by:

$$\rho_{nf} = (1-\phi)\rho_f + \phi\rho_s$$

The thermal expansion coefficient of the nanofluid can be determined by:

$$(\rho\beta)_{nf} = (1-\phi)(\rho\beta)_f + \phi(\rho\beta)_s$$

The specific heat capacity of nanofluid is:

$$(\rho c_p)_{nf} = (1-\phi)(\rho c_p)_f + \phi(\rho c_p)_s$$

The effective thermal conductivity of a fluid for the two-component spherical particle suspension can be determined by Maxwell-Garnett's approximation model:

$$\frac{k_{nf}}{k_f} = \frac{(k_s + 2k_f) - 2\phi(k_f - k_s)}{(k_s + 2k_f) + \phi(k_f - k_s)}$$

For validation, the results of the numerical results for average Nusselt number in a square cavity are compared with the results of other researches. The comparison is shown in Table 2 which shows a very good agreement.

Table2. Comparison between present work and other published data

	$10^4$	$10^5$	$10^6$
<b>Present work</b>	2.241	4.526	8.919
<b>de Vahl Davis [9]</b>	2.243	4.519	8.8
<b>House et a.l [10]</b>	2.254	4.561	8.923
<b>Merrickh and Lage [11]</b>	2.244	4.536	8.86

**RESULTS AND DISCUSSION**

**1- The cavity with an attached baffle to the bottom wall**

Figure 2 shows the isotherms and streamlines of the cavity with a baffle attached to its bottom wall. The baffle is located at  $d=0.3$  and height of the baffle is considered to be 0.2, 0.5 and 0.8 and Rayleigh number is  $Ra=10^5$ .

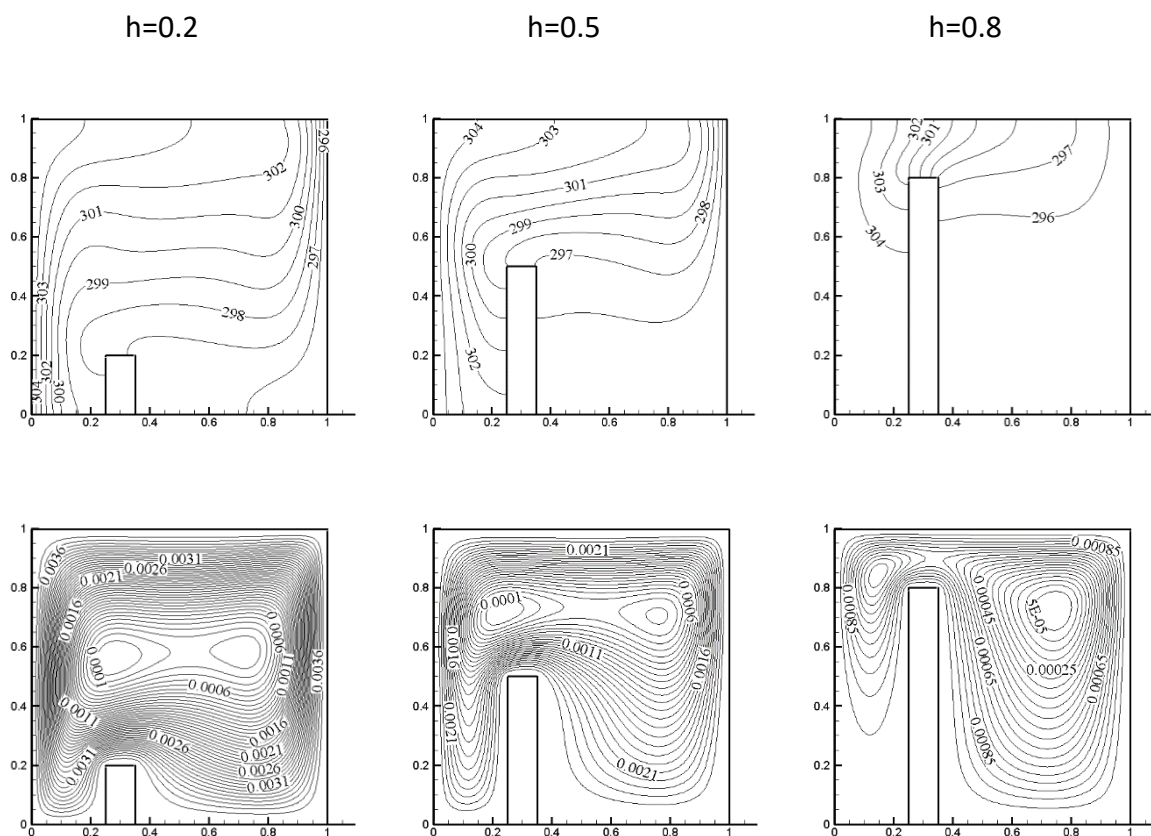


**Figure2.** The effect of the variation of baffle height attached to the bottom wall. Isotherms and Streamlines for  $d=0.3$ ,  $Ra=10^5$ ,  $\phi = 10\%$

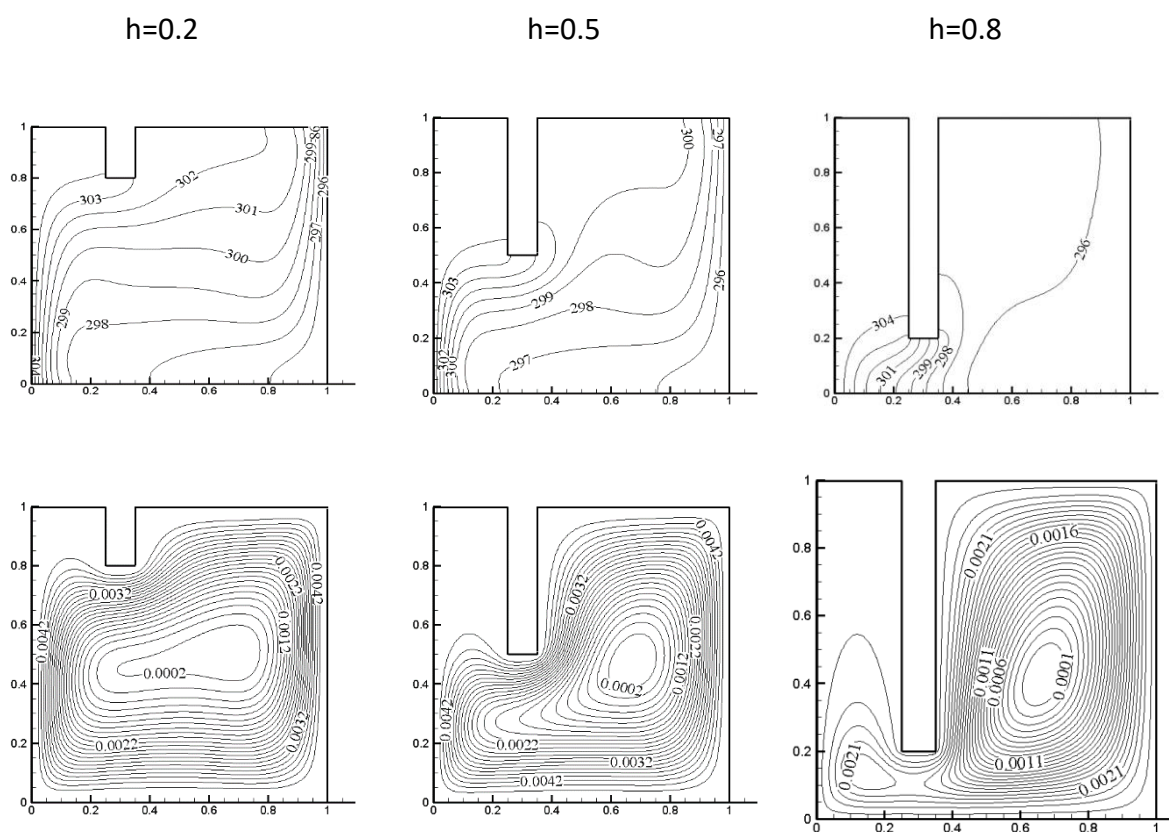
According to the figures, it is found that the effect of the baffle with  $h=0.2$  is mostly changing the local temperature distribution and the other parts of the cavity have got no effects. This phenomenon can be explained in this way that the initial vortex has not changed considerably with the presence of the baffle with  $h=0.2$  and baffle has just affected the local velocity. In the middle parts of the cavity, as the conduction heat transfer is predominant the lines are horizontal but in the areas next to hot and cold areas, the lines are vertical which shows the predominance of the convective heat transfer. When the distance between the top and bottom decreases with the increase of the baffle height, the congestion of the isothermal lines is observed in this

distance. The congestion of the isotherms is a sign of better heat transfer in this area. With the baffle height increasing, the low temperature area next to the cold wall and the high temperature area next to hot wall increase because the natural direction of the flow will be confined for the presence of the baffle. In the lower heights, because of the higher convective heat transfer flow, better distribution of isothermal lines is observed. The graphs make it clear that by reaching  $h=0.8$ , the separation of the hot area and cold area is appeared.

The streamline show that lower height of the baffle has not caused great effect on the fluid flow. The two holes-which are the center of the flow circulation- display this fact that some of the fluid particles could not remove heat from hot wall and transfer it to the cold wall. As the height of the baffle goes up, these small holes become more. The presence of the baffle is a barrier in front of the heat and flow transfer. Therefore, according to graphs, it is noticed that with the rising of baffle height, streamlines in the hot side move to upper part of the cavity because the high baffle does not allow the heat to be transferred in the lower parts of the hot wall which leads to the separation of the flow to hot and cold areas. The graphs apparently show that in  $h=0.2$  and  $0.5$ , big vortices are formed which cover hot and cold areas but in  $h=0.8$ , as there is not enough space for heat transfer, except some, most of the vortices are formed in hot or cold areas. Moreover, increase in the baffle height causes the reduction of the streamline strength.

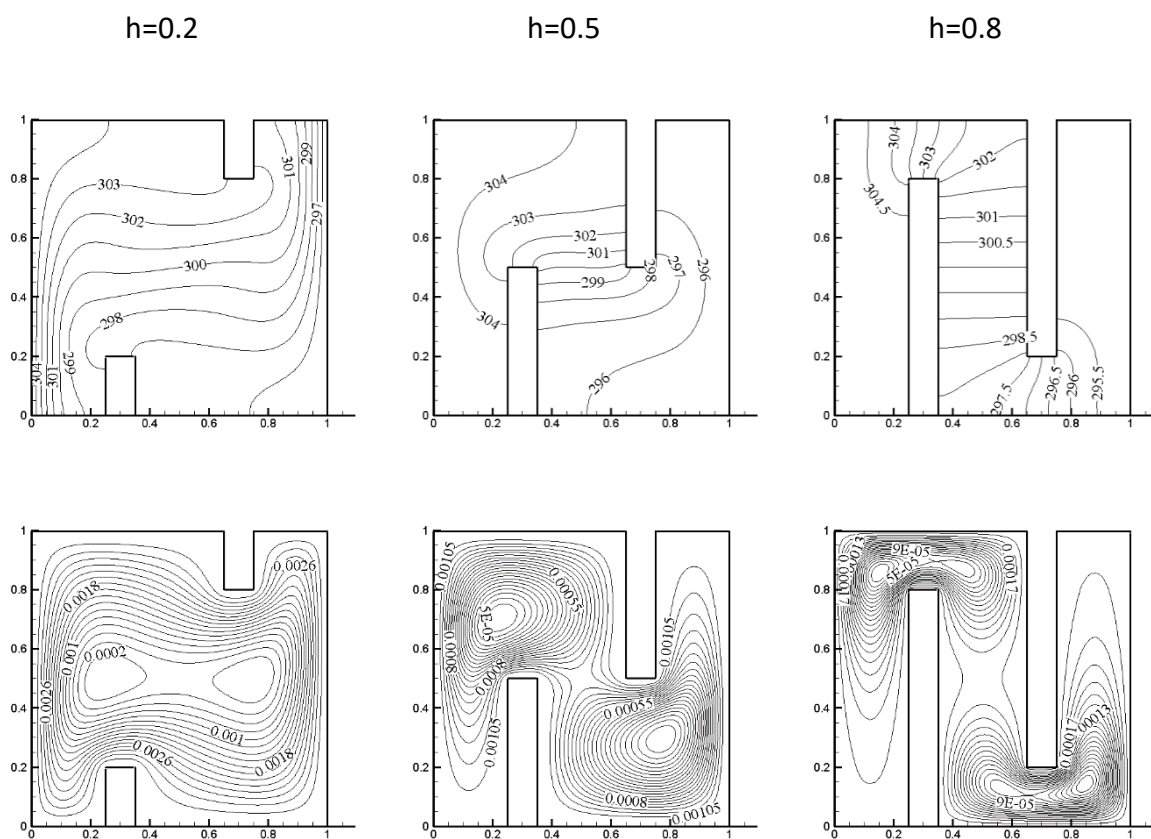
### 2- Cavity with an attached baffle to top side

Figure 3 depicts the cavity in which an insulated baffle is attached to its top wall. Because of the symmetry characteristic, the results are similar to the cavity with an attached baffle to the bottom side.



### 3- Cavity with two baffles attached to top and bottom sides

Figure 4 shows the isothermal and streamlines for the cavity with two baffles which have been placed with the same distance  $d=0.3$  from the hot and cold walls. Like other studied cavities, baffles with  $h=0.2$  have not influenced the cavity flow a lot. For  $h=0.5$ , isothermals have curves in the top left and bottom right parts but they are horizontal between the two baffles. It is happened as convection heat transfer is higher in top left and bottom right part of square but between the two baffles because of the separation, heat transfer is weak. According to the streamlines, it is clear that great amount of the flow is in the space between the baffles and insulated walls. The initial big vortices that have been formed for lower baffle heights, tend to separate in the center of the cavity and compared with the previous studied case, the power of the stream is decreased as the height of baffle increases. For the maximum studied height, in the vortical areas, the isothermal lines are disappeared but for the confined fluid between the two baffles, these lines are seen as bulk. This fact happens because the circulation of the fluid in the vortical areas makes the temperature difference lower whereas is higher for the confined fluid. It is also seen that in the distance between baffles and the top and bottom walls, the lines are compressed and vertical but are horizontal between the two baffles. These patterns show this fact that the confined fluid prevents the heat transfer from the hot wall to the cold wall and conductive heat transfer is just considered in the central part of the cavity. For this height, the streamlines show complete separation of the flow and the compression of the streamlines is the sign of the predominance of conductive heat transfer.



## CONCLUSION

A numerical study has been performed to investigate the effect of baffle height on the natural convection in a cavity having isothermal vertical walls and adiabatic horizontal walls filled with Al<sub>2</sub>O<sub>3</sub>-water based nanofluid. The main conclusions of the present analysis are as follows. The results show that heat transfer decreases considerably with increasing partition height. In the lower heights, the baffle is mostly changing the local temperature distribution and fluid flow and the other parts of the cavity have got no effects. Moreover, because of the higher convective heat transfer flow, better distribution of the isothermal lines is observed. Furthermore, increase in the baffle height causes the reduction of the streamline strength.

## REFERENCES

- [1] Choi US.1995. Enhancing thermal conductivity of fluids with nanoparticles developments and application of non-Newtonian flows. ASME Journal of Heat Transfer. 66: 99-105.
- [2] Khanafer K, Vafai K and Lightstone M. 2003. Buoyancy- driven heat transfer enhancement in a two-dimensional enclosure utilizing nanofluids. International Journal of Heat and Mass Transfer. 46: 3639-3653.
- [3] Tian YS, Karayiannis TG. 2000. Low turbulence natural convection in an air filled square cavity. Part I: the thermal and fluid flow fields. International journal of heat and mass transfer. 43: 849–866.
- [4] Santra AK, Sen S and Chakraborty N. 2008. Study of heat transfer augmentation in a differentially heated square cavity using copper-water nanofluid. International Journal of Thermal Science. 47: 1113-1122.
- [5] Putra N, Roetzel W and Das SK. 2003. Natural convection of nanofluids. Heat Mass Transfer. 39: 775- 784.
- [6] Anilkumar SH and Jilani G. 2008. Convective Heat Transfer Enhancement in an Enclosure with Fin Utilizing Nano Fluids. World Academy of Science, Engineering and Technology. 43: 98.
- [7] Habibzadeh A, Sayehvand H and Mekanik A. 2011. Numerical Study of Natural Convection in a Partitioned Square Cavity Filled with Nanofluid. International Journal of Chemical Engineering and Applications. 2: 269-274.
- [8] Sayehvand H, Habibzadeh A and Mekanik A. 2012. CFD analysis of natural convection heat transfer in a square cavity with partitions utilizing Al<sub>2</sub>O<sub>3</sub> nanofluid. International Journal of Nano Dimensions. 2: 191-200.
- [9] De Vahl Davis G. 1983. Natural convection in a square cavity: A benchmark numerical solution. International Journal of Numerical Methods Fluids. 3: 249–264.
- [10] House JM, Beckermann C and Smith TF. 1990. Effect of a centered conducting body on natural heat transfer in an enclosure. Numerical Heat Transfer. 18: 213–225.
- [11] Merrikh AA and Lage JL. 2005. Effect of distributing a fixed amount of solid constituent inside a porous medium enclosure on the heat transfer process. International Journal of Heat and Mass Transfer. 48: 4748–4765.



## Single walled carbon nanotubes reinforced intermetallic TiNi matrix nanocomposites by spark plasma sintering

Badis Bendjemil<sup>1,2</sup>, Mahiedinne Ali-Rachedi<sup>3</sup>, Jamal Bougdira<sup>4</sup>, Faming Zhang<sup>5,6</sup>, Eberhard Burkel<sup>5</sup>

<sup>1</sup>LASEA, Dept of Chemistry, University of Badji-Mokhtar, 23000 Annaba, Algeria

<sup>2,3</sup>Department of Mechanical Ingeniering , University of 8 Mai 1945 Guelma, 24000 Guelma, Algeria

<sup>3</sup>Department of Mechanical Ingeniering, Faculty of Engineering Sciences, University of Badji-Mokhtar, Annaba, Algeria

<sup>4</sup>Institut of Jean Lamour, UMR 7198 CNRS - University of Lorraine, Faculty of Sciences and Technologies, BP 70239 F-54506 Vandoeuvre les NANCY cedex, France

<sup>5</sup>Physics of New Materials, Institute of Physics, 18055 Rostock, Germany

<sup>6</sup>School of Materials Science and Engineering, Southeast University, 211189 Nanjing, China

\*)E-mail: [Badis23@ymail.com](mailto:Badis23@ymail.com)

Received 19 march. 2016; Revised 22 march 2016; Accepted 1 May 2017

We report the processing of single walled carbon nanotubes (SWCNTs) reinforced TiNi intermetallic matrix nanocomposites from Ti/Ni and SWCNTs powders using spark plasma sintering (SPS) at temperatures from 1000 °C to 1200 °C. The SWCNTs are doped into the TiNi matrix from 0.0 to 1.0 wt%. The effect of SWCNTs reinforcement contents on the relative density, phases, microstructure and microhardness of TiNi intermetallics matrix and CNTs/TiC/TiNi nanocomposites are studied. The experimental results show that the TiNi sintered at T= 1200 °C reinforced with 0.8 wt% SWCNTs has the highest Vicker's microhardness and relative density, which were HV 5.29 GPa and 96%, respectively. That can be explained by the precipitation of TiC and Ti<sub>2</sub>Ni in the matrix. This study explores the possibility of developing novel TiNi matrix nanocomposites with shape memory effect and biocompatibility.

**Keywords:** Intermetallic-matrix composites (IMCs), SWCNTs-reinforcement, Structural properties, Spark plasma Sintering, Nanocomposites, Mechanical properties

**PACS:** 73.30.+y, 73.40.Ns, 73.40.-c.

## **1. Introduction**

TiNi shape memory alloys have exceptional properties, such as the shape memory effect, pseudoelasticity and biocompatibility, which enable them to be widely used in numerous applications [1]. Recent research works have shown that TiNi alloys exhibit better wear resistance than many conventional tribological materials due to their pseudoelasticity [2, 3]. Their rapid work hardening, good corrosion and fatigue resistance may also be beneficial [4]. Besides its equiatomic concentration, it is well known for its shape memory effect (SME). Due to its unique physical and mechanical properties at room temperature ductility, damping effect, corrosion resistance and biocompatibility, TiNi shape memory alloys can be used for biomedical applications [5, 6]. Porous TiNi-shapememory alloy has, for example, been considered as a promising biomedical material for orthopedics and bone implant surgeries in recent years [7].

A pulse current pressure sintering equipment was used for the consolidation at various sintering temperatures of TiNi alloy powder prepared by mechanical alloying [8]. A bulk Ni–Ti material with refined microstructure was obtained by spark plasma sintering (SPS) starting from amorphous mechanically alloyed NiTi powders [9]. It has also been made to develop TiNi matrix composites to further increase the wear resistance. The reinforcing phases include TiC [10], TiN [11] and precipitated Ti<sub>2</sub>Ni [12], it is considered that the hard reinforcing phases can be used to sustain external load, while the TiNi matrix may accommodate deformation, absorb impact energy and retain hard particles.

Carbon nanotubes (CNTs) are considered to be the most effective reinforcement in metal–matrix composites for structural applications [13], [14], [15], [16], [17], [18], [19], [20] and [21] due to their extraordinary mechanical, thermal, and electrical properties and high aspect ratios. In the past, 1 vol% CNTs/TiNi composites with enhanced compressive properties and wear resistance have been fabricated by hot-press sintering [22]. The tensile properties of these CNT/TiNi composites have also been reported [23]. However, the strengthening effects of CNTs and any further effects on the shape memory of the composite have not been examined. Additionally, the five volume ratio of the CNTs has resulted in insufficient strain for measuring the shape memory effect of the CNTs/NiTi composites.

In this paper, we describe the preparation of CNTs-reinforced TiNi matrix composites through a powder metallurgical process using CNTs, and Ni and Ti elemental powders. Spark plasma sintering (SPS), which requires a very short time to sinter metal and ceramic powders, was applied to consolidate the CNTs/TiNi composite powder at elevated temperatures at 1000 and 1200 °C with and without addition from 0.4 to 1.0 wt% of (SWCNTs). The microstructure of each composite was observed, the density was determined, and its mechanical properties were studied. The chemical compositions (at.%) of the unreinforced specimen and matrix are designed as 50% Ti–50% Ni. Carbon nanotubes (CNTs) reinforced TiNi matrix nanocomposites were synthesized by spark plasma sintering (SPS) employing elemental powders. The phase structure, morphology and transformation behaviors were studied. Attempts have also been made to develop CNTs-TiNi matrix nanocomposites to further application in biomedical and shape memory effect. The effect of the CNTs on the mechanical properties and density of the nanocomposites was investigated.

## 2. Experimental procedure

As starting materials, commercially available powders of Ti (<45 micrometer, 99.7% purity), Ni (<10 micrometer, 99.9% purity, high purity Aldrich, Germany) were used with sizes of around 40 micrometer, respectively. The Ti, Ni and single-walled carbon nanotubes (SWCNTs with diameter < 2 nm) powders were mixed in a stoichiometric molar ratio of 1:1 with addition of SWCNTs in the range of 0.4 to 1.0 wt % by ball milling, and then dried in a vacuum. Fig.1 presented the starting sintering powder.

The mixtures were loosely compacted into a graphite die of 20 mm in diameter and sintered in vacuum (1 Pa) at various temperatures (1000–1200 °C) using an SPS apparatus (Tycho lab SINTER, FCT-HP-D5, FCT, Germany) (Fig.2, Table 1).

**Table 1:** Synthesis parameters of the sintered Nanocomposite TiNi/CNTs

Samples	T (°C)	T (min)	Heating rate (°C/min)	P (MPa)	50Ti-50Ni with wt% SWCNTs d=1nm	Current (A)
SPS1	1200	20	100	60	00	3000
SPS2	1200	20	100	60	0.8	3000
SPS3	1000	20	100	60	0.4	3000
SPS4	1100	20	100	60	0.0	3000

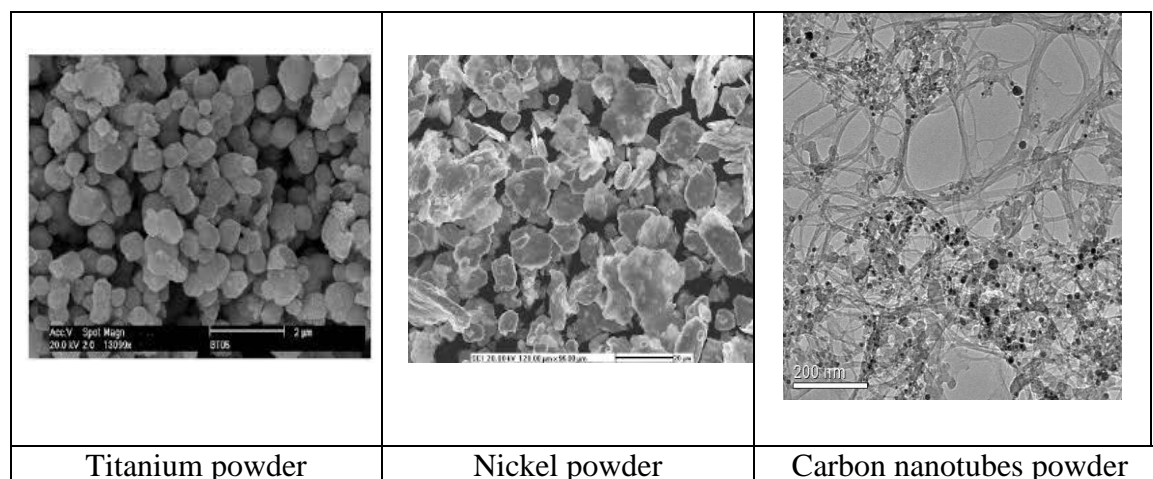


**Figure 1.** Starting powders before sintering.



**Figure. 2.** TYCHO SINTER, SPS-1050, Sumitomo Coal Mining Co. Ltd., Rostock, GERMANY.

A constant heating rate of 100 °C/min was employed, while the applied pressure was 60 MPa. The on/off time ratio of the pulsed current was set to 12/2 in each run. The maximum current reached approximately 3000 A during sintering. The soaking time at high temperatures was within 10 min. The mixed powders used for sintering were obtained from ball milling and heterogeneous coacervation methods. The unreinforced sample and a composite with an SWCNT weight fraction of SWCNTs were fabricated by SPS at 1000, 1100 and 1200 °C under a pressure of 60 MPa and total cycle of 20 min. The sintered sample was polished and the density was determined.

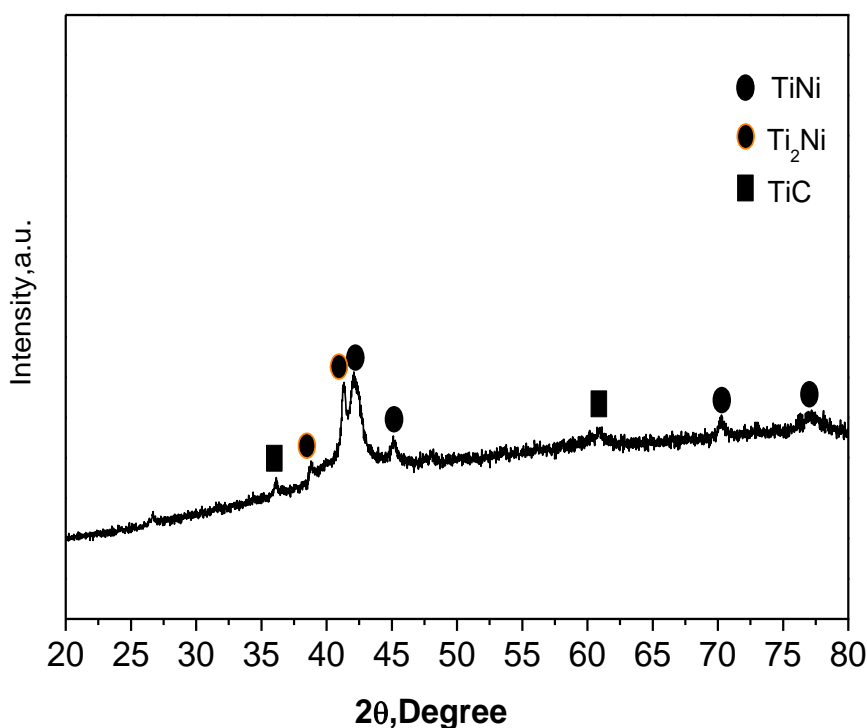
The phase identification and the preferred orientation of the TiNi reinforced SWCNTs crystalline grains were evaluated by X-ray diffraction analysis by Bruker (Type D4, GmbH) using Cu K $\alpha$  radiation in the angular range of  $2\theta = 20\text{--}80$  degrees at a step rate of 0.020 s to identify the crystalline phases of the sintered samples at room temperature. The morphology of the elemental powders' particles and the microstructure of the sintered specimens were determined with a scanning electron microscope (FESEM Tscan Vega, GmbH). The optical and FESEM micrographs were used to determine the porosity of the sintered specimens by MIP Microstructural Analysis Processing Software. The product was cut along the cylindrical axis by Archimedes' method using water immersion. The microhardness at the top surface and the

lateral surface were measured by a diamond Vickers hardness tester. The indentation loads, ranging from 10 to 500 N, were applied for 20 s for each measurement.

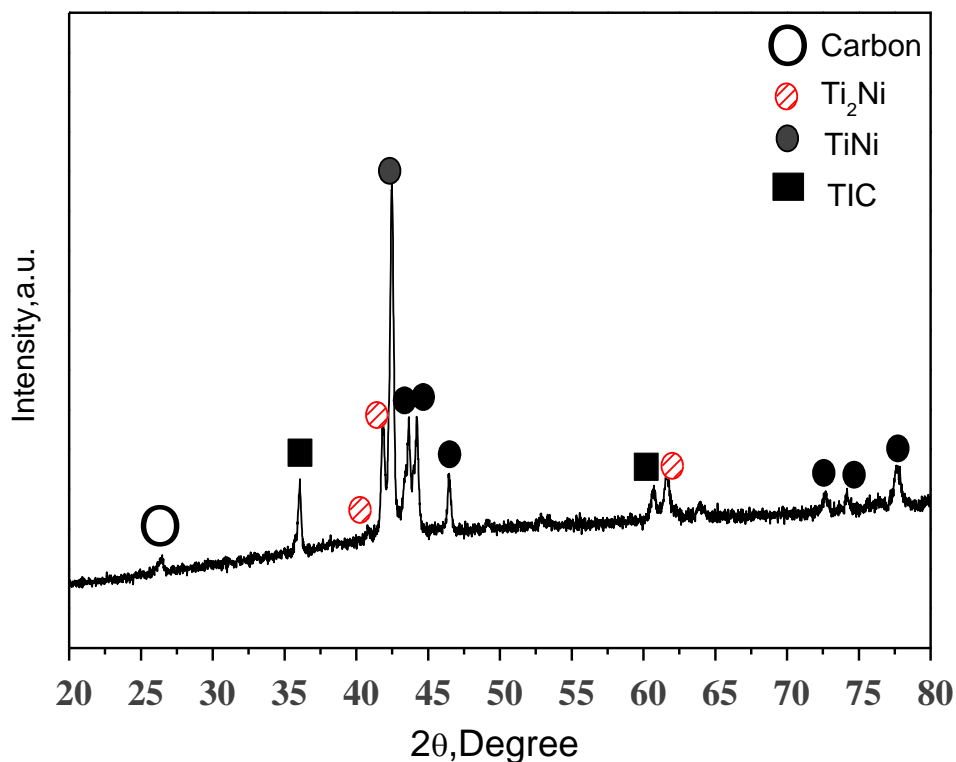
### 3. Results and discussion

#### 3.1. XRD analysis of powders and sintered TiNi-SWCNTs nanocomposites

Figure 3, 4, and 5 shows the XRD spectrum of the pure TiNi and the reinforced nanocomposite by SWCNTs. It can be seen that the main phase is the TiNi phase, and precipitated TiC, Ti<sub>2</sub>Ni phases co-exist in the three samples. XRD patterns of the TiNi, and the nanocomposites are shown in Fig. 5. The Ti<sub>2</sub>Ni phase was formed during the sintering process in all of the samples because it is a thermodynamically favorable phase at the sintering temperature compared with TiNi phase [17]:

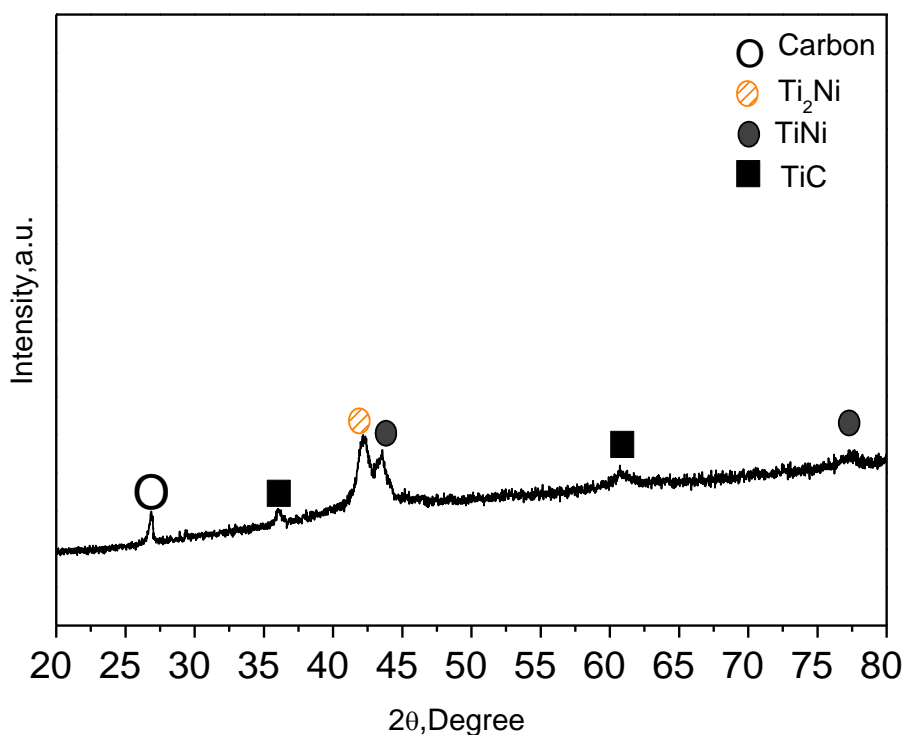


**Figure. 3.** XRD spectra of unreinforced TiNi sintered at T=1200°C (SPS<sub>1</sub>)



**Figure. 4.** XRD spectra of reinforced TiNi-CNTs nanocomposites produced at T=1200°C reinforced with 0.8 wt% SWCNTs (SPS<sub>2</sub>)

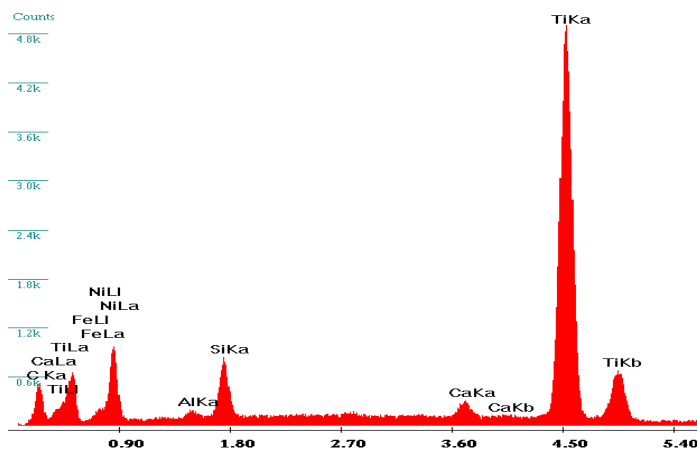
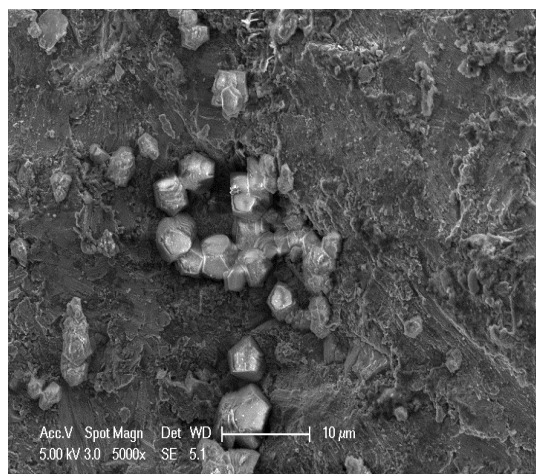
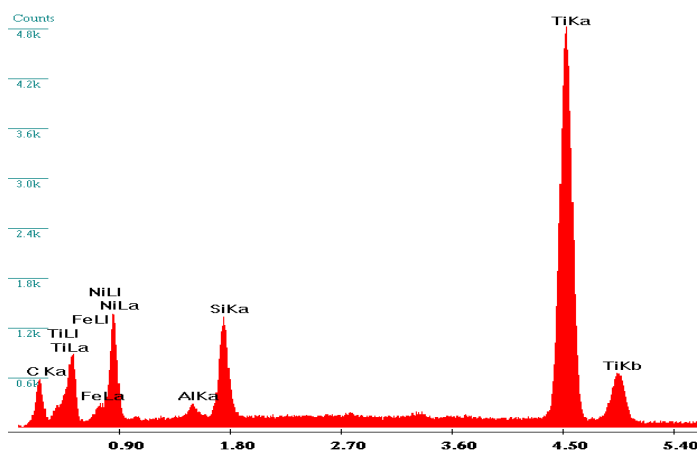
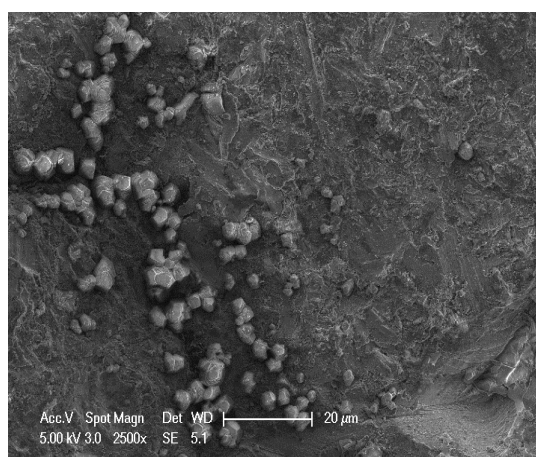
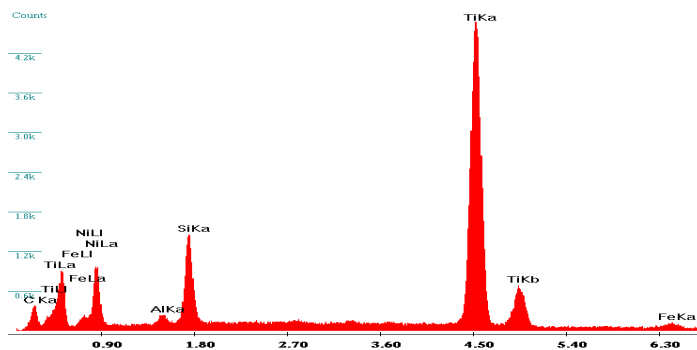
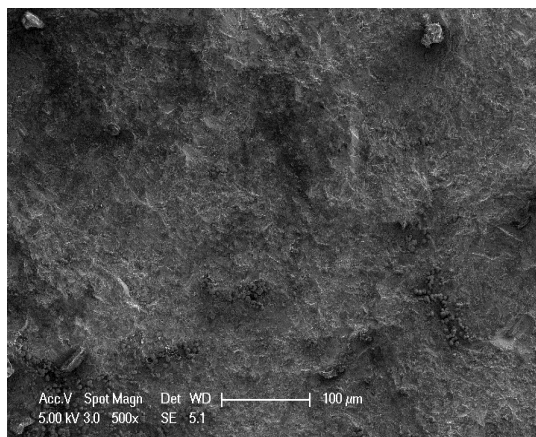
XRD spectrum of the nanocomposite, indicates that the reaction between the Ti powders and SWCNTs did happen during the sintering process. This reaction has been previously observed [24], and it is considered that disordered carbons on wall defects and the open ends of the SWCNTs serve as carbon sources for interfacial reaction. The sintered samples consisted mainly of TiNi matrix, as major phases, and some secondary phases, such as TiC and Ti<sub>2</sub>Ni, appeared depending on the sintering temperature. X-ray diffraction patterns of sample (0.8 Wt% CNTs-TiNi matrix nanocomposites) sintered at 60 MPa pressure were enhanced because they were reinforced with three phases, TiC, Ti<sub>2</sub>Ni and SWCNTs with higher intensity is shown in Fig. 3, 4 and 5. Fig. 3 shows the SWCNTs content as a function of sintering temperature, which was reduced to 5 wt% when sintered at 1200 °C for 10 min at 60 MPa pressure because it reacted with Ti to produce TiC new reinforcement.



**Figure. 5.** XRD spectra of TiNi-CNTs nanocomposites produced at  $T=1000^{\circ}\text{C}$  reinforced with 0.4 wt% SWCNTs (SPS<sub>3</sub>)

### 3.2. FESEM microstructural observation of sintered CNTs-TiNi nanocomposites

The worn surfaces and wear debris are compared in Figure 5. The Microstructural and EDS analysis displays elemental analyses of the various regions of the sintered samples, TiNi, and the CNTs/TiC/TiNi nanocomposites in chemical composition (at.%) (Fig. 6, 7 and 8). It can be seen that, with the addition of CNTs reinforcements, the contents of Ti, Ni and O in the sintered samples decrease. According to the above results, it can be concluded that the wickers hardness has been improved by adding SWCNTs.



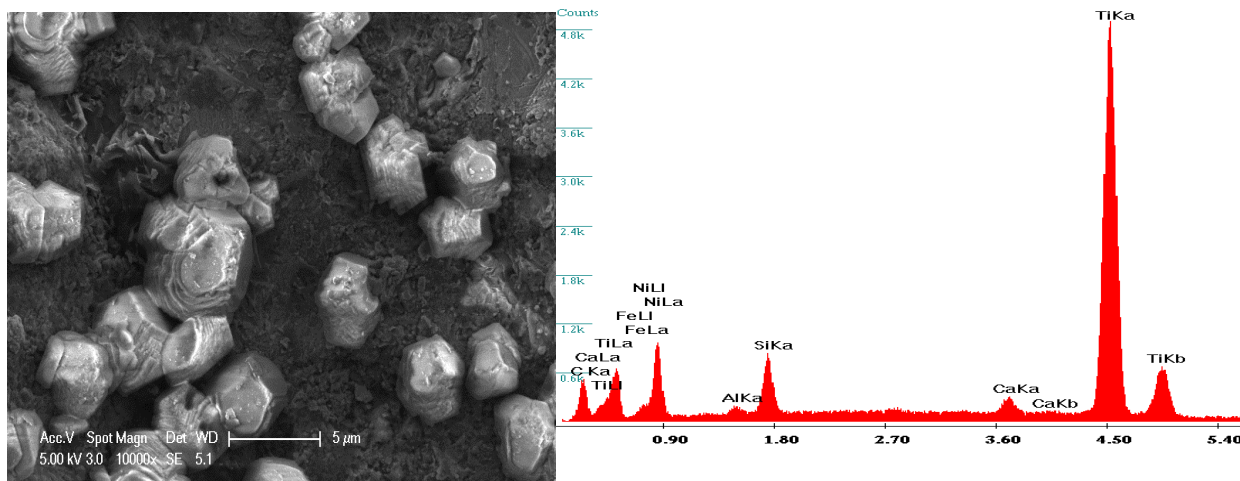
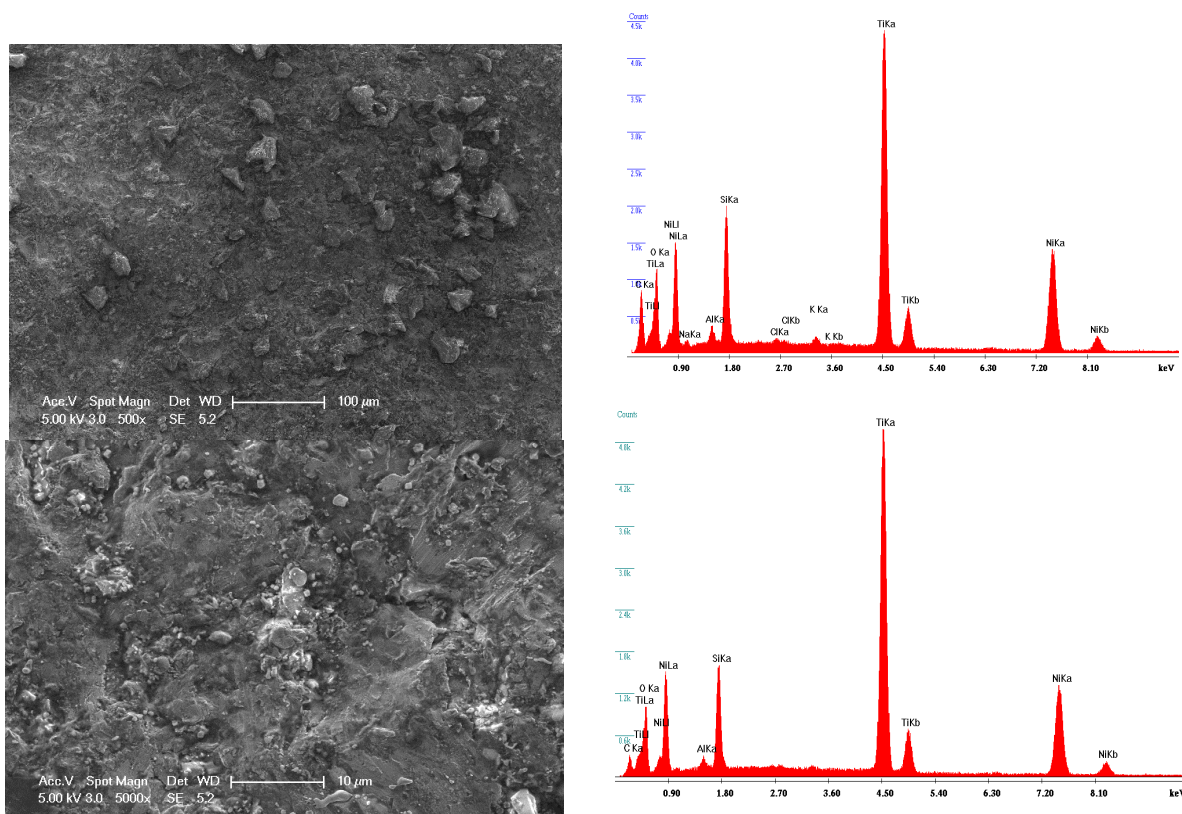
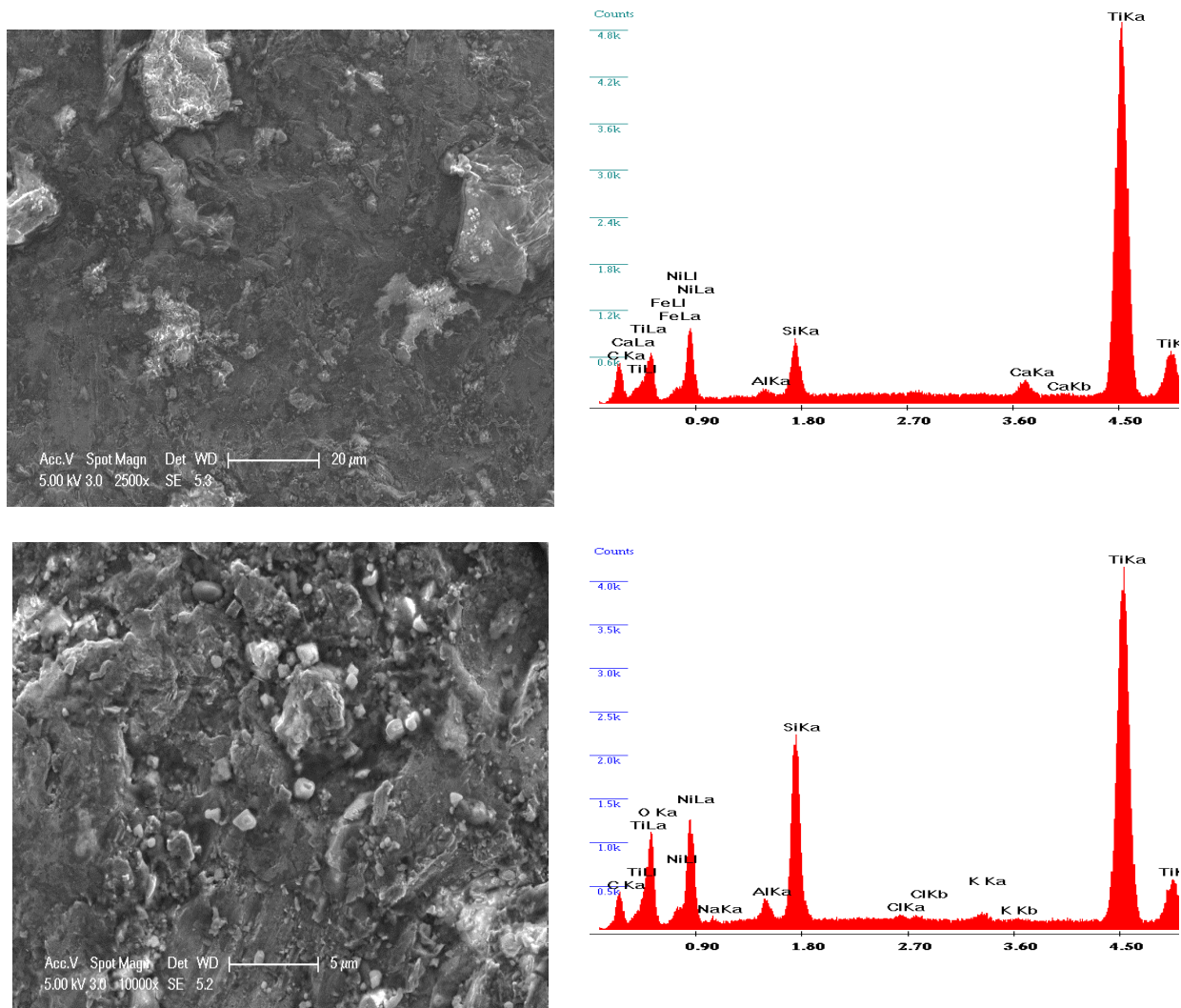
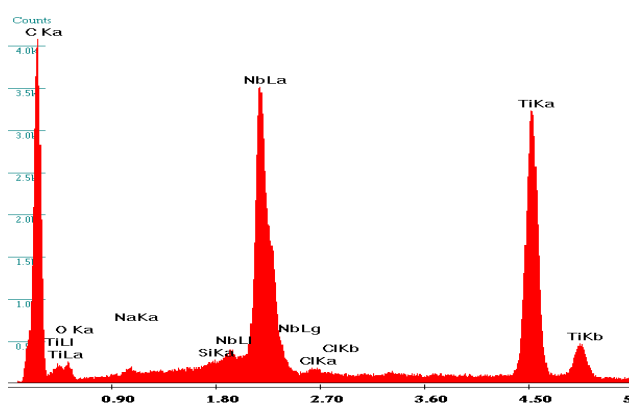
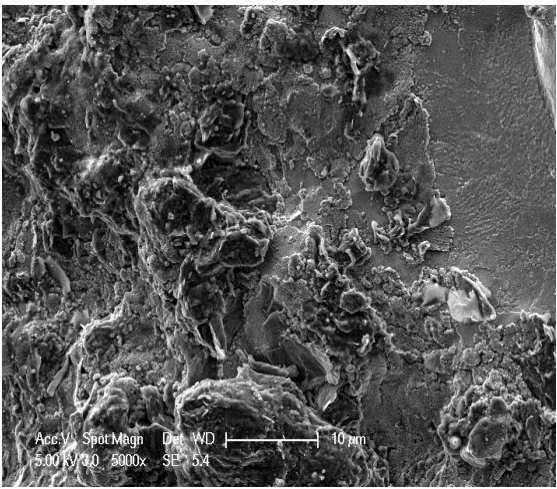
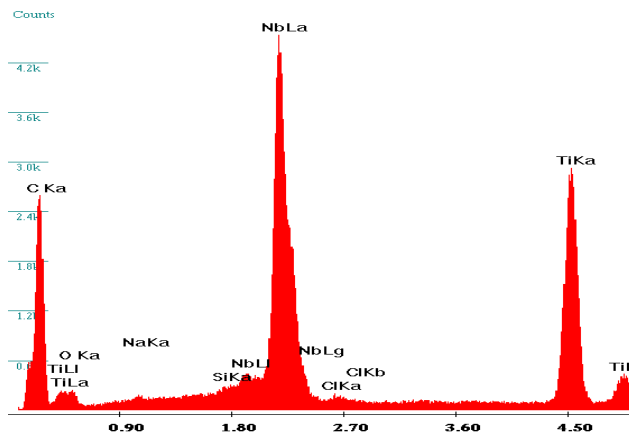
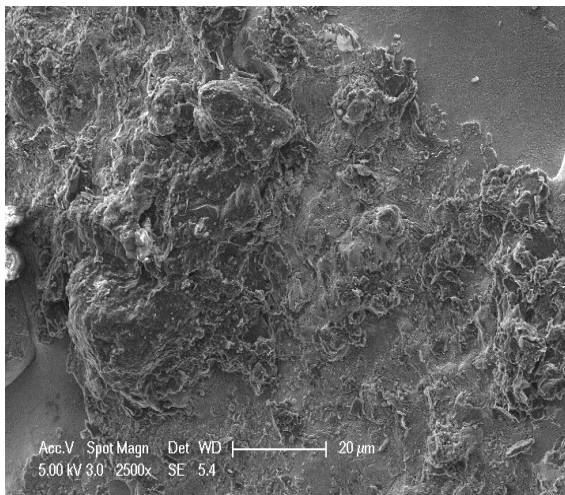
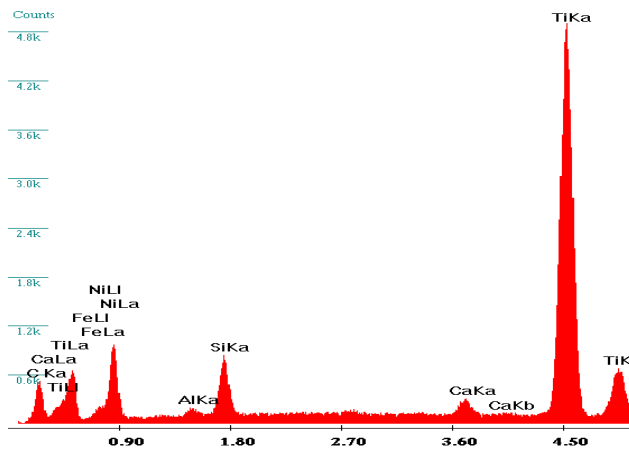
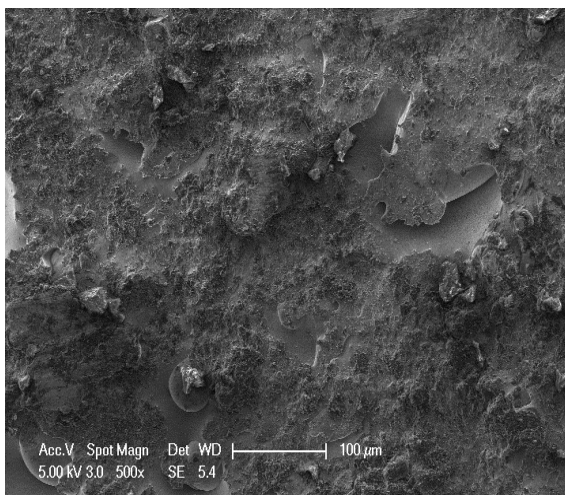


Figure. 6. Micrographs from the worn surfaces of unreinforced TiNi produced at T=1200°C





**Figure. 7.** FESEM micrographs from the worn surfaces of TiNi-CNTs nanocomposites produced at T=1200°C reinforced with 0.8 wt% SWCNTs



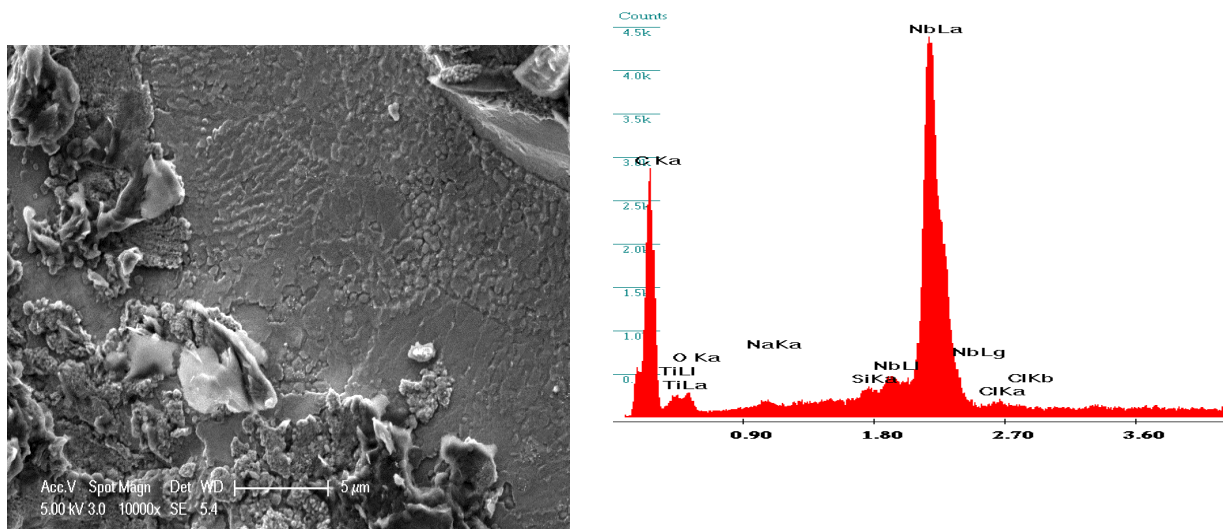


**Figure. 8.** FESEM micrographs from the worn surfaces of TiNi-CNTs nanocomposites produced at T=1000°C reinforced with 0.4 wt% SWCNTs

Figure. 7 shows the microstructure and the EDS spectra of the TiNi, and the CNTs/TiC/TiNi nanocomposites. EDS spectra was used to determine the elemental composition of the different regions in the sample and are presented by the red spectra. The SEM micrographs in Fig. 7 shows a dark phase that corresponds to the TiNi matrix phase, and a lighter phase that corresponds to Ti<sub>2</sub>Ni which exists mainly at the grain boundary, TiC is represented by the agglomerat in cubique polycrystal form in addition to unreacted CNTs [16].

### 3.3. Relative density and microstructure

The variation of the relative density of sintred TiNi and TiNi–CNTs nanocomposites with SWCNTs reinforcement is shown in Fig. 9. The theoretical density of the composite used for obtaining relative density was calculated using a rule of mixture using the densities of two of the constituent phase ( $\rho_{TiNi} = 6.55 \text{ g cm}^{-3}$ ,  $\rho_{SWCNTs} = 2.25 \text{ g cm}^{-3}$ ) with the given SPS processing paramaters, the TiNi sample exhibited best densification with relative density greater than 98%, with the similar prosscassing parameters and variation of temperature CNTs–TiNi nanocomposites.

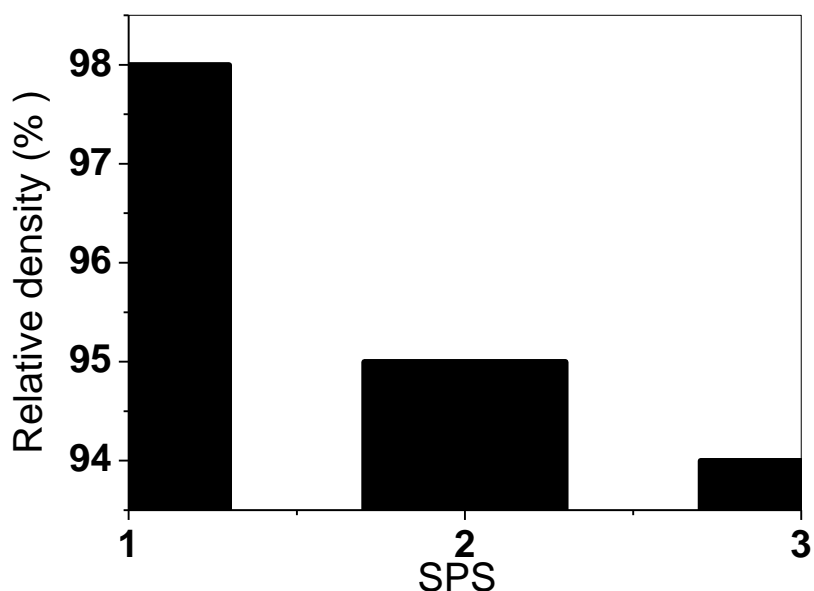


**Figure. 9.** Relative densities of the TiNi–CNTs nanocomposites as a function of SWCNTs reinforcement content (SPS<sub>1</sub>) (SPS<sub>2</sub>) (SPS<sub>3</sub>)

The relative density decreased with increasing wt% CNTs reinforcement. The TiNi–SWCNTs nanocomposites 0.8 wt% CNTs at T=1200 °C exhibited relative density of about 95%. Clearly, the CNTs reinforcement makes the densification of CNTs–TiNi nanocomposites more difficult. This seems to be the direct consequence of higher melting point of SWCNTs (T=3160 °C) compared to that of TiNi (T=3000 °C). XRD analysis indicated formation of new intermediate phase TiNi<sub>2</sub> from the action between Ti and Ni, while the intensities of SWCNTs peaks remained unchanged.

Depending on the final density to be achieved, the SPS operating condition were properly chosen, that is, 750 °C, 5 MPa for 5 min, to obtain a relative density of 75 %, 800 °C, 25 MPa for 5 min, for samples 87 % dense, and 850 °C, 50 MPa for 5 min, for zero porosity compacts. The 13% porosity sample exhibited a round microstructure with high ductility, while the 25% porous product displayed much lower stress flow as compared to that of the 13 % porosity [24]. Also, the easy sledding of their walls when attached by weak van der Waals force of coalesced MWCNTs can probably decrease the relative density.

### 3.4. Microhardness

Fig. 10 presents the variation of Vickers microhardness of CNTs-TiNi nanocomposites with CNTs reinforcement content. The microhardness of the composites increased almost linearly with increasing SWCNTs reinforcement content. The hardness of SWCNTs (28–30 GPa) is nearly 7–8 times the previously reported values of hardness of TiNi (4 GPa). For the nearly single phase TiNi -SPS sintered in this investigation, the microhardness was found to be 5.96 GPa (measured with indentation load of 10 N), which is higher than the previously reported hardness values for monolithic [22]. While the higher hardness of the TiNi sample

could be due to minor amounts of SWCNTs phase in the TiNi sample, it could also be due to indentation size effects. It was reported that the hardness decreases with increasing load and asymptotically approaches a value of 2 GPa at higher loads. The microhardness in the range of about 2.5–3.5 GPa

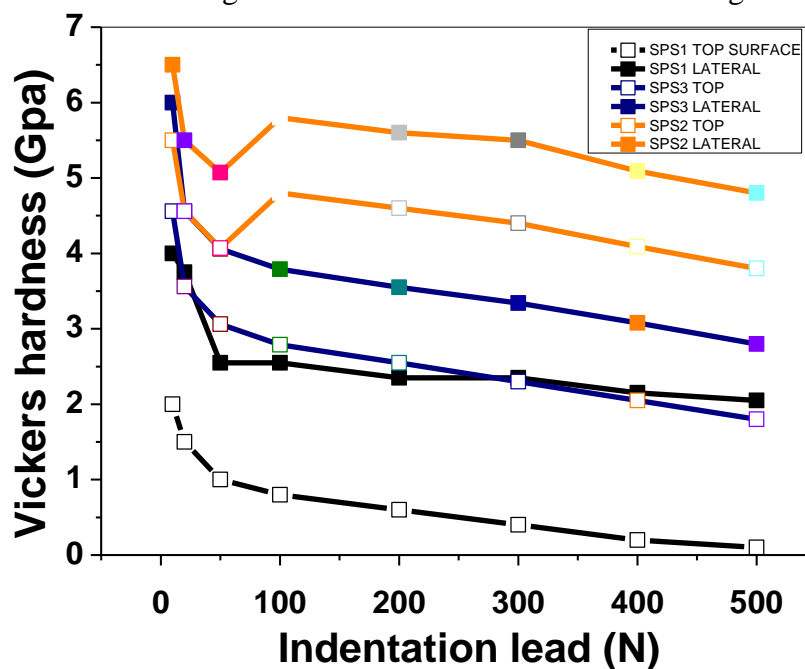


**Figure. 10.** Vickers microhardness of TiNi–CNTs nanocomposites as a function of SWCNTs reinforcement content (SPS<sub>1</sub>) (SPS<sub>2</sub>) (SPS<sub>3</sub>)

was found for lower loads (10 N). The TiNi–SWCNTs nanocomposites reinforced with 0.8 wt% of SWCNTs exhibited the highest hardness of about 5.5–6.5 GPa. A slight increase in average hardness have been obtained from TiNi matrix nanocomposites prepared by sintering 0.8 wt % single-walled carbon nanotubes (SWCNTs) with Ti and Ni elemental powders. It is considered that *in situ*, TiC and the remaining SWCNTs act as reinforcements and plays a major role in the improvement. Finally, the unreacted SWCNTs (Fig.6) coalesced to MWCNTs function of the temperature and process the highest hardness. It is believed that a large recoverable strain will lead to a low maximum contact pressure, and the deformation recovery can also diminish plastic deformation and retard crack propagation, thus minimizing the surface damage [18]. The formation of TiC is function of the temperature and CNTs reinforcement as carbon source. Also, the improvement of compressive mechanical and tribo nanocomposite, properties will be tested. The memory effect and bionanocomposite compatibility will also be performed in the near future.

### 3. Conclusion

Dense CNTs–TiNi nanocomposites with varying weight fraction of coated CNTs were fabricated successfully by SPS in the range of 1000, 1100, and 1200 °C under a pressure of 60 MPa for 20 min in pure Ar atmosphere protection. The TiNi with 0.8 wt% SWCNTs had the

highest Vicker's microhardness and relative density, which were HV 5.29 GPa and 96%, respectively. This increased with the addition of CNTs. Although TiC was formed by reaction of CNT and Ti, unreacted CNTs could be found. Mechanical properties of TiNi were enhanced by unreacted CNTs.

### **Acknowledgements**

We are grateful to Prof. Jaafar Gambaja, Drs. Damien Genève and Ghouti Medjeldi (Institut Jean Lamour, University of Henri Point Carré, Nancy, France) for the help in FESEM and XRD investigations.

### **References**

- [1] T. Duerig, A. Pelton, D. Stockel. *Mater Sci Eng A* 273–275(1999)149.
- [2] N.B. Morgan *Mater Sci Eng A* 378 (2004)16.
- [3] Kujala Sauli. Biocompatibility and biomechanical aspects of nitinol shape memory metal implants. Finland: Department of Surgery, Department of Anatomy and Cell Biology, University of Oulu press; (2003).
- [4] K. Otsuka, X. Ren, *Progress in Materials Science* 50 (2005) 511–678.
- [5] M. Abedini, H.M. Ghasemi, M.N. Ahmadabadi, *Materials Characterization* 61 (2010) 689–695.
- [6] M. Abedini, H.M. Ghasemi, M.N. Ahmadabadi, *Materials Science and Technology* 26 (2010) 285–288.
- [7] Y. Shida, Y. Sugimoto, *Wear* 146 (1991) 219–228.
- [8] L. L. Ye, Z.G. Liu, K. Raviprasad, M. X. Quan, M. Umemoto, Z.Q. Hu, *Mater. Sci. Eng.A* 241 (1998) 290-295.
- [9] A. Teray ama, H. Kyogoku, M. Sakamura, S. Komatsu, *Mater. Trans.* 47 (2006) 550–557.
- [10] H.Z. Ye, R. Liu, D.Y. Li, R. Eadie, *Scripta Mater.*, 41 (1999) 1039–1045
- [11] Y.C. Luo, D.Y. Li, *Journal of Materials Science*, 36 (2001)4695–4702.

- [12] X. Hu<sup>a</sup>, Y.F. Zheng, Y.X. Tong, F. Chen, B. Tian, H.M. Zhou, L. Li, *Materials Science and Engineering: A* 623(2015)1–3
- [13] T. Kuzumaki, K. Miyazawa, H. Ichinose, K. Ito, *J. Mater. Res.*, 13 (1998)2445–2449.
- [14] H. Kwon, M. Estili, K. Takagi, T. Miyazaki, A. Kawasaki, *Carbon*, 47 (2009)570–577.
- [15] W.A. Curtin, B.W. Sheldon, *Mater. Today*, 7 (2004)44–49.
- [16] E.T. Thostenson, Z.F. Ren, T.W. Chou, *Compos. Sci. Technol.*, 61 (2001)1899–1912.
- [17] W.X. Chen, J.P. Tu, L.Y. Wang, H.Y. Gan, Z.D. Xu, X.B., Zhang *Carbon*, 41 (2003) 215.
- [18] S.I. Cha, K.T. Kim, S.N. Arshad, C.B. Mo, S.H. Hong, *Adv. Mater.*, 17 (2005)1377.
- [19] D.H. Nam, S.I. Cha, B.K. Lim, H.M. Park, D.S. Han, S.H. Hong, *Carbon*, 50 (2012)2417.
- [20] K.T. Kim, S. Il Cha, S.H. Hong, S.H., *Mater. Sci. Eng. A – Struct.*, 430 (2006)27.
- [21] Y.J. Jeong, S.I. Cha, K.T. Kim, K.H. Lee, C.B. Mo, S.H., 3 (2007) 840.
- [22] X. Feng, J.H. Sui, W. Cai, A.L. Liu., *Scr. Mater.*, 64 (2011)824.
- [23] X. Feng, J.H. Sui, W. Cai., *J. Compos. Mater.*, 45 (2011)1553.
- [24] Yeon-wook Kim , *Materials Letters*162 (2016) 1–4.



## Structural, magnetic, electric and electronic aspects of the $\text{Ba}_2\text{YbSbO}_6$ perovskite material

L.A. Carrero Bermúdez, R. Moreno Mendoza, R. Cardona, D.A. Landínez Téllez, J. Roa-Rojas\*

*Grupo de Física de Nuevos Materiales, Departamento de Física, Universidad Nacional de Colombia, A.A. 5997, Bogotá DC, Colombia.*

\*}Email : jroar@unal.edu.co

Received 19 march. 2016; Revised 22 march 2016; Accepted 1 May 2017

A single crystallographic phase of the  $\text{Ba}_2\text{YbSbO}_6$  perovskite was synthesized by the solid-state reaction method. From the refinement of the XRD pattern it was obtained that this sintered material crystallizes in a rhombohedral complex perovskite, R-3 (#148) space group. SEM images showed the sub-micrometric character of its granular surface. Measurements of susceptibility as a function of temperature evidenced the antiferromagnetic behavior of this material below the Néel temperature  $T_N=118$  K and a paramagnetic feature above this critical temperature. The magnetic parameters were obtained from the fitting of susceptibility in the paramagnetic regime with the Curie-Weiss equation. From theoretically calculated Density of States and band structure the semiconductor characteristic of the material was determined and the energy gap was predicted for the up and down spin orientations of the electron gas close to the Fermi level. The energy gap value was experimentally corroborated from diffuse reflectance spectra with the Kubelka-Munk fit of the experimental result. Measurements of dielectric constant as a function of applied frequencies at room temperature reveal a decreasing behavior.

**Keywords:** Perovskite, characterization, electronic structure.

**PACS:** 61.66.Fn; 68.37.Hk; 75.50.Ee; 77.22.-d; 71.20.Ps.

### 1. Introduction

In the last years the complex perovskites with generic formula  $\text{A}_2\text{BB}'\text{O}_6$  [1-3] have been subject of enhanced scientific studies because the wide range of applications that these materials present on an industrial scale. Double perovskites belonging to the series  $\text{Ba}_2\text{LnB}'\text{O}_6$  (Ln=lanthanide and  $\text{Y}^{3+}$  and  $\text{B}'=\text{Nb}^{5+}$ ,  $\text{Ta}^{5+}$ ,  $\text{Sb}^{5+}$ ) are of interest due to their potential use as substrates for high- $T_c$  superconductors [4,5] and their likely high chemical compatibility with the structurally analogous, oxygen deficient double perovskites,  $\text{Ba}_2\text{LnSnO}_6$ , which is a series of interest for use as solid state electrolytes due to their high ionic conductivity [6,7]. Substitution of

$Nb^{5+}$ ,  $Ta^{5+}$ ,  $Sb^{5+}$  could provide a method of controlling the oxygen stoichiometry of these compounds, potentially minimizing the problems caused by reduction of  $Ba_2LnSnO_6$  that is thought to be a consequence of the large level of oxygen vacancies in these compounds [6]. Phase transitions in perovskites have long been of interest to solid-state chemists [8]. Previous studies [9, 10], using laboratory X-ray and medium resolution neutron diffraction, reported that the structures in the series  $Ba_2LnSbO_6$  change from  $R\bar{3}$  rhombohedral (tilt system  $a^-a^-a^-$ ) to  $Fm\bar{3}m$  cubic ( $a^0a^0a^0$ ) symmetry with decreasing size of the  $Ln^{3+}$  cation. That the symmetry increases as the ionic radius of the lanthanide decreases, this is consistent with the increase of the tolerance factor, which in double perovskites is given by  $\tau = \frac{r_A+r_O}{\sqrt{2}\left(\frac{r_B+r_{B'}}{2}+r_O\right)}$ , where  $r_A$ ,  $r_B$ ,  $r_{B'}$  and  $r_O$  are the ionic radii of the  $A$ ,  $B$ ,  $B'$ , and  $O$  ions, respectively [11]. An increase in the tolerance factor indicates that the volume of the  $BO_6$  octahedron is better matched to the size of the  $AO_{12}$  polyhedron reducing the need for the octahedral tilting to accommodate this A-site cation. Since octahedral tilting is responsible for the lowering of the symmetry from cubic, the symmetry tends to increase, as the B-type cation gets smaller. The aim of this work is to carry out a detailed *ab initio* theoretical study of the  $Ba_2YbSbO_6$  material, which belongs to this interesting complex perovskite family, and establish a correlation with experimental results of crystalline structure, electric behavior, magnetic response and energy gap. The understanding of these properties is essential in order to elaborate a comprehensive scheme of the potential application of the rare earth Sb-based double perovskites.

## 2. Experimental procedure

The  $Ba_2YbSbO_6$  samples were produced by the solid-state reaction method, from oxide powders of  $Yb_2O_3$ ,  $Sb_2O_5$  and  $Ba_2CO_3$  (Aldrich 99.9%), which were stoichiometrically mixed according to the chemical formula  $Ba_2YbSbO_6$ . Then, the resultant mixture was grinded and pressed to form a pellet of 9.0 mm diameter and annealed at 1000 °C for 30 h. The samples were then remacerated, repelletized and sintered at 1100 °C for 40 h and 1200 °C for 40 h. The crystalline structure was studied from X-ray diffraction (XRD) by means of a PW1710 diffractometer ( $\lambda_{CuK\alpha}=1.54064 \text{ \AA}$ ). Rietveld refinement of the experimental data was performed through the GSAS code [12]. Morphological surface studies were carried out by means scanning electron microscopy (SEM) experiments by the utilization of a VEGA 3 electronic microscope. Field cooling measurements of the magnetic susceptibility as a function of temperature were studied by using a MPMS Quantum Design SQUID. Diffuse reflectance experiments were performed by using a VARIAN Cary 5000 UV-Vis-NIR spectrophotometer, which has an integration sphere with a PMT/Pbs detector. The value of the relative dielectric constant was established by using an Agilent HP4194A-350 frequency analyzer.

## 3. Calculation method

The electronic and band structures were predicted from the application of the Full-Potential Linear Augmented Plane Wave method (FP-LAPW) within the framework of the Kohn-Sham Density Functional Theory (DFT) [13]. The exchange and correlation effects were treated by using the Generalized Gradient Approximation (GGA) [14]. This potential considers the difference between the electronic densities for the two distinct spin orientations from the beginning. The self-

consistent process was developed by the numeric package Wien2k [13]. Taking the experimental unit cell data as input (with a formula unit), the structure studied in this work were fully relaxed with respect to their lattice parameters and the internal degrees of freedom compatible with the space group symmetry of the crystal structure. The resulting energies versus volume functions have been fitted to the equation of state due to Murnaghan [15] in order to obtain the minimum energy value, the bulk modulus, its pressure derivative and the equilibrium lattice parameters and associated volume. The muffin-tin radii used for  $\text{Ba}_2\text{YbSbO}_6$  were 2.20, 2.50, 2.12 and 1.82 Bohr for Ba, Yb, Sb and O respectively, angular momentum up to  $l = 10$  inside the muffin-tin sphere, a maximum vector in the reciprocal space of  $G_{\text{max}} = 12.0$ . Energy convergence tests were performed and  $RMT * K_{\text{max}} = 7.0$  was selected for calculations. A mesh of 1000 points in the first Brillouin zone (equivalent to a maximum of 250  $k$  points in the irreducible Brillouin zone) was used. Finally, the convergence criterion for the self-consistent calculation was 0.0001 Ry for the total energies and 1.0 mRy/u.a. in the internal forces. Spin polarization was included in the calculations.

#### 4. Results and discussion

The refined experimental pattern of XRD result for  $\text{Ba}_2\text{YbSbO}_6$  is shown in figure 1. The black line represents the experimental data and red line corresponds to the simulated pattern by means of the GSAS code. Base line is the difference between theoretical and experimental results. Refinement parameters of figure 1 were  $\chi^2 = 7.613$ ,  $R_{(F2)} = 6.04\%$ . The Rietveld refinement permitted to establish that this material adopts a rhombohedral perovskite structure, which belongs to the  $R-3$  (#148) space group. The lattice parameter obtained from the refinement is  $a = 5.9104 \text{ \AA}$  with trigonal angle  $\alpha = 59.9993^\circ$ . These results are 99.0% in agreement with the theoretical values obtained from the Structure Prediction Diagnostic Software *SPuDS* [16], which predicts  $a = 5.9672 \text{ \AA}$  and  $\alpha = 59.6389^\circ$ .

The found structure corresponds to the  $a-a-a-$  tilt system in the Glazer notation. The crystallization of  $\text{Ba}_2\text{YbSbO}_6$  in the  $R-3$  (#148) space group can be corroborated taking into account that the XRD pattern corresponding to this symmetry involves reflections, signaling odd-odd-odd reflections, which is characterized by cationic ordering and simple octahedral tilting.

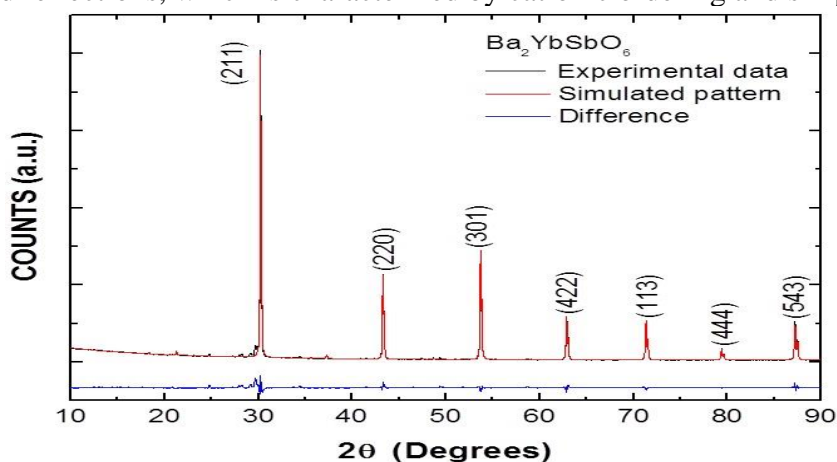


Figure. 1: Characteristic XRD pattern for the  $\text{Ba}_2\text{YbSbO}_6$  double perovskite. Symbols represent experimental diffraction data, continuous lines are the simulated patterns and base line is the difference between experimental and calculated values.

In the study and description of crystallographic structures the concept of *positions* is fundamental [17]. Then, the so called Wyckoff positions for this structure were experimentally determined to be  $Ba=2c$ ,  $Yb=1a$ ,  $Sb=1b$  and  $O=6f$ . In this notation,  $a$ ,  $b$ ,  $c$  and  $f$  are the Wyckoff letters that determine all the points  $x$  for which the site-symmetry groups are conjugate subgroups of the  $R-3$  [18]. These letters constitute just a coding frame for the Wyckoff positions, starting with  $a$  at the bottom position and continuing in alphabetical order [17]. The number of equivalent points per unit cell, which accompanies the letter of Wyckoff, is known as multiplicity of the Wyckoff position. In the case of the  $R-3$  (#148) space group, the Wyckoff letter  $a$  has a unique possible coordinate  $(0,0,0)$  and therefore its multiplicity is 1. In the same way,  $b$  has  $(\frac{1}{2},\frac{1}{2},\frac{1}{2})$ . On the other hand,  $c$  has multiplicity 2, because this position may have coordinates  $(x,x,x)$  and  $(-x,-x,-x)$ . For this Wyckoff position we have obtained  $(\frac{1}{4},\frac{1}{4},\frac{1}{4})$ . At last,  $f$  has multiplicity 6, with possible coordinates  $(x,y,z)$ ;  $(z,x,y)$ ;  $(y,z,x)$ ;  $(-x,-y,-z)$ ;  $(-z,-x,-y)$  and  $(-y,-z,-x)$ . In our case the position  $(-0.2256, -0.2997, 0.2628)$  was obtained.

The tolerance factor calculated from the experimental data is  $\tau=0.9335$ , which is in accordance with expected values for the trigonal perovskite structures [16]. From the refinement analysis the octahedral distribution in the structure of the  $Ba_2YbSbO_6$  material was constructed showed in figure 2. In this figure a marked difference between the orientation of the  $Yb-O_6$  and  $Sb-O_6$  octahedra is perceived. This octahedral disorientation is due to differences in the ionic radii of the cations  $Yb^{3+}$  and  $Sb^{5+}$ , as well as to the differences between the links of the two cations in their octahedral coordination with the oxygen anions.

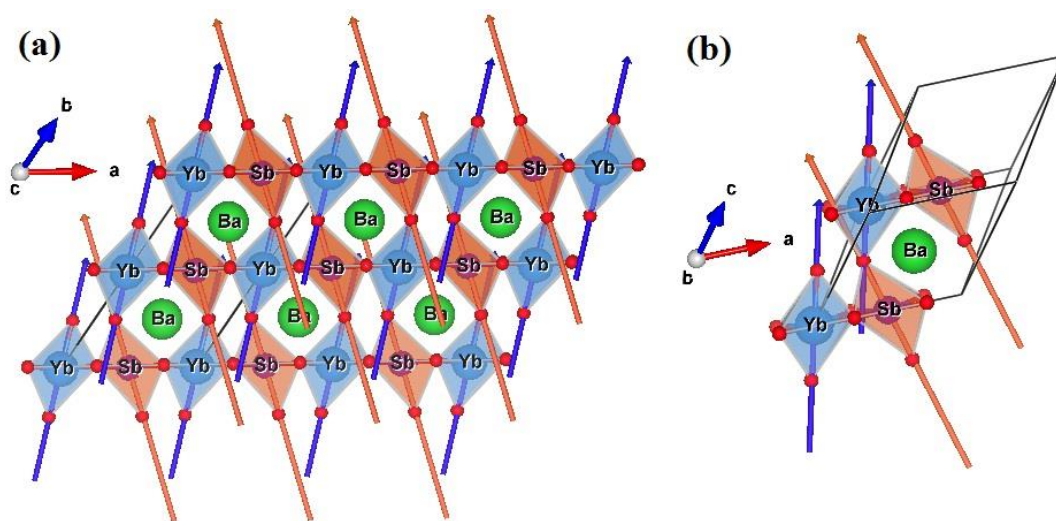


Figure. 2: Structure of the  $Ba_2YbSbO_6$  for the  $R-3$  space group in the planes (a)  $ab$  and (b)  $ac$ .

An important observation about the structural distortion is related to the tilt angle of the octahedra, which is obtained to be  $\beta_{Yb}=17.965^\circ$  for  $Yb-O_6$  and  $\beta_{Sb}=-16.887^\circ$  for  $Sb-O_6$ , for a total deviation of  $34.852^\circ$  between their directions.

SEM image of the material shown in figure 3 reveals a qualitative approximation to the surface microstructure. In picture 3a evidences the formation of clusters of polyhedral grains and interstitial particulate grains. By applying the intercept technique in picture 3b, it is clear that the grains could end up having a few tenths of a micron, form groups, which have appearance of clusters over  $2 \mu\text{m}$ .

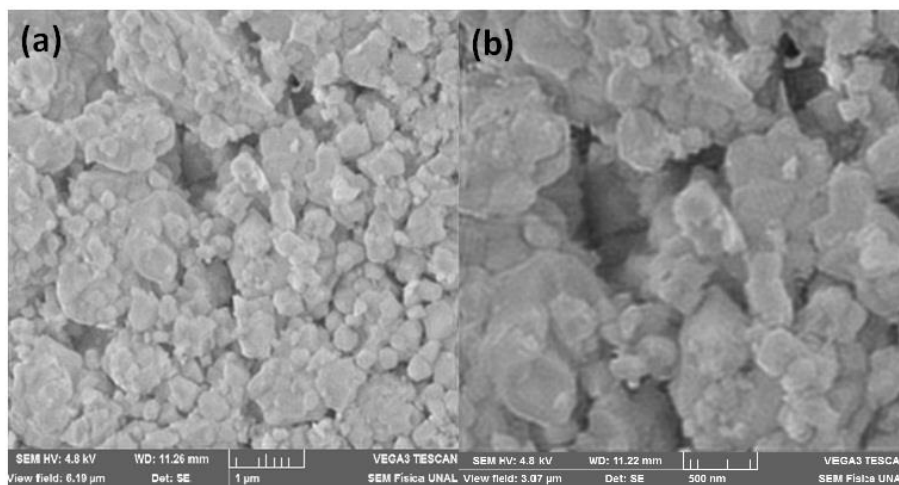


Figure. 3. SEM images of  $\text{Ba}_2\text{YbSbO}_6$  for magnifications (a) 32500x and (b) 65000x.

From measurements of magnetic susceptibility as a function of temperature the magnetic response of the  $\text{Ba}_2\text{YbSbO}_6$  complex perovskite was examined. As observed in figure 4, the magnetic behavior of this material has a paramagnetic signature at high temperatures.

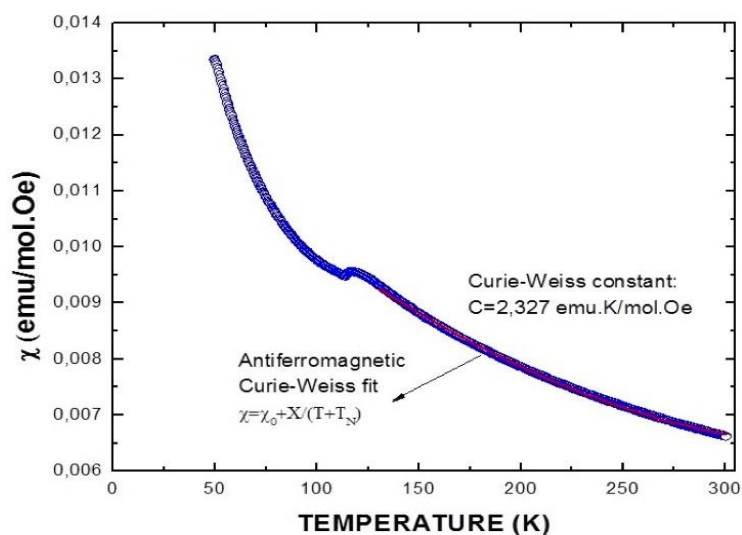


Figure. 4. Magnetic susceptibility as a function of temperature measured for the  $\text{Ba}_2\text{YbSbO}_6$  material.

Magnetic parameters were obtained from the Curie-Weiss equation  $\chi = \chi_0 + \left(\frac{C}{T+T_N}\right)$ , where  $C = \frac{N\mu_{eff}^2}{3K_B} = 2,327 \text{ emu.K/mol.Oe}$  is the Curie constant,  $N$  is Avogadro's number,  $\mu_{eff}$  is the effective magnetic moment ( $\mu_{eff} = P_{eff}\mu_B$ ),  $P_{eff}$  represent the effective Bohr magneton number,  $\mu_B$  is the Bohr magneton,  $K_B$  is the Boltzmann constant and  $\chi_0 = 0,00439 \text{ emu/mol.Oe}$  is the temperature independent susceptibility term. From the Curie constant  $C$  the effective magnetic moments for  $\text{Ba}_2\text{YbSbO}_6$  material was calculated to be  $4,31 \mu_B$ . This value is 95% in agreement with the theoretical expected moment obtained from the Hund's rules for the  $\text{Yb}^{3+}$  isolated cation as  $g\sqrt{J(J+1)} = 4,54 \mu_B$  [19]. The Néel temperature  $T_N = 118 \text{ K}$  was obtained from the Curie-Weiss fitting of the experimental data. We notice that the anomaly observed in figure for  $T = 118 \text{ K}$  is directly related with the critical temperature of magnetic ordering.

Because the antiferromagnetic behavior obtained from the fitting of the experimental data to the Curie-Weiss equation, three different antiferromagnetic configurations (AFM1, AFM2 and AFM3) were analyzed in order to study the electronic structure of the Yb and Sb sub-lattices, as shown in figure 5. The minimum energy configuration was obtained by the optimization of the atomic positions and the cell parameter settings for each magnetic configuration, using variable cell relax calculation based on the experimental lattice parameters. Since the AFM1 is the most stable configuration wherein the antiferromagnetic coupling exists between (001) crystallographic planes of  $\text{Ba}_2\text{YbSbO}_6$  hereinafter, only this configuration was considered for the density of states calculations.

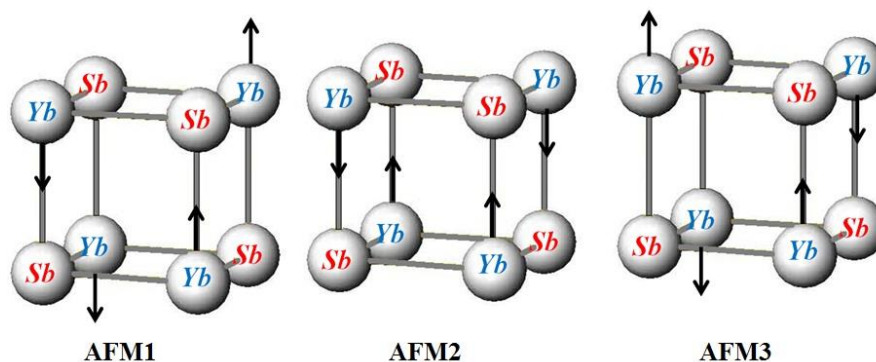


Figure. 5. Antiferromagnetic configurations considered for the study of the electronic structure in the  $\text{Ba}_2\text{YbSbO}_6$  perovskite material.

Figure 6 shows the band structure (a) and Total Density of States (b) for the  $\text{Ba}_2\text{YbSbO}_6$  complex perovskite for both down and up spin polarizations. It is observed in the picture that this material behaves as semiconductor of indirect gap through the Fermi level (energy gap  $E_g=2.3 \text{ eV}$ ) for the spin down polarization and conductor with for the other. It is important to elucidate that the scales are not similar for 6a and 6b pictures. In other words, for the spin down orientation the valence band is majority due to the *Yb* orbital contributions close to the Fermi level. On the other hand, for the up spin polarization, the valence and conduction band are continuous across the Fermi level but also due to the *Yb* orbital contributions. In the conduction band a set of available states are sited in the energy value  $2.25 \text{ eV}$  and corresponds to *O* contributions.

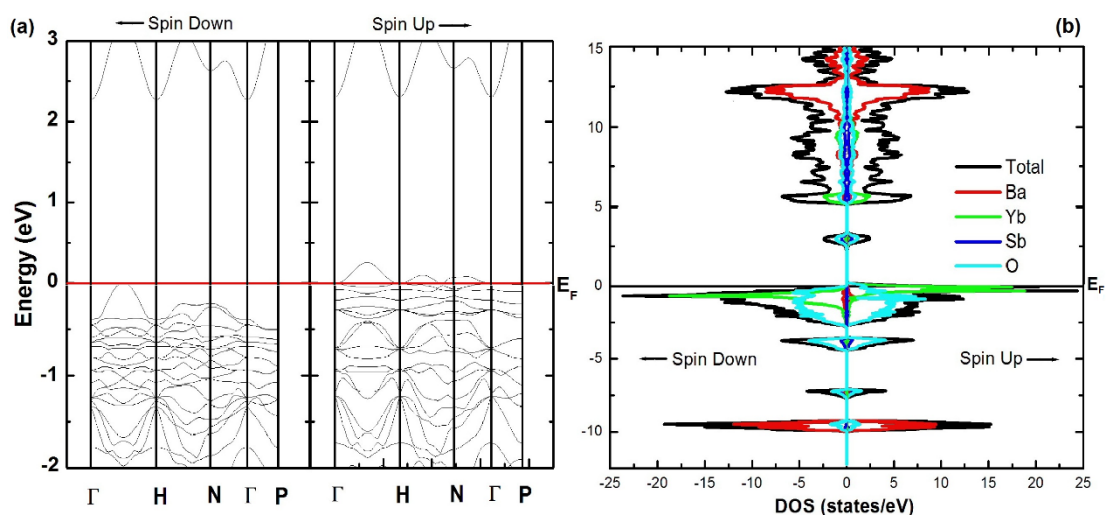


Figure. 6. Band structure (a) and Total Density of States (b) for down and up spin polarizations.

Figure 7a exemplifies the partial Density of States calculated for the *Yb*, *Sb*, *Ba* and *O* separate ions. On the other hand, figure 7b exemplifies the contribution of several *Yb* and *O* orbital to the Density of States close the fermi level. From these pictures it is clear that close to the Fermi level the *Yb-4f* orbital are responsible for the conductor behavior for the spin up orientation and the semiconductor character for the spin down polarization. *O-2p* orbital has an incipient contribution in the valence band but a relative contribution in the localized states of the conduction band. Magnetic moment of mixed charge density was calculated from the asymmetry of the *Yb-4f* states close the Fermi level.

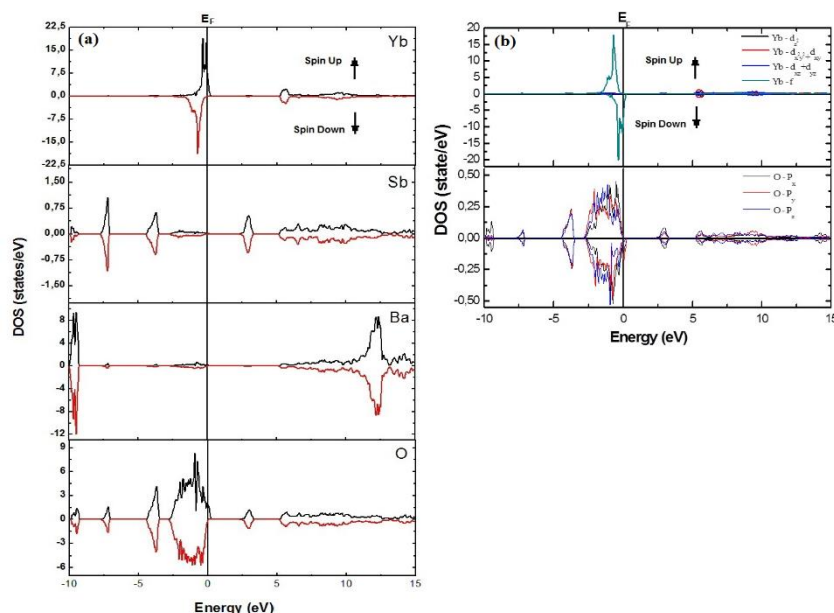


Figure. 7. Partial Density of States for (a) the Yb, Sb, Ba and O ions, and (b) Yb and O orbital. Fermi level is identified in E=0 eV.

Total magnetic moment in cell was determined to be  $5.0 \mu_B$  for  $Ba_2YbSbO_6$ . This result is 14% higher than the experimentally obtained. However, an important element to be taken into account has to do with the clutter of *Yb* and *Sb* cations in the structure of the double perovskite, which can not only distorted octahedra but also modify the magnetic response of the material. The integer theoretical value of the effective magnetic moment and the conductor characteristics of the band structure for the spin up states and semiconductor for the others suggest a tendency of this material to a half-metallic behavior [20].

Results of diffuse reflectance experiments are shown in figure 8a. In the picture, reflectance values experimentally acquired with a step of  $1 \text{ nm}$  over the  $300\text{--}2500 \text{ nm}$  range are schematized. From the absorption of UV-Vis-NIR radiation it was observed that the molecules of the  $Ba_2YbSbO_6$  material cause the weak excitation of electrons from the ground state to excited state. The radiated energy, the quantum characteristics energy dependent from the electronic configuration was calculated. As presented in figure 8b, from the adjustment to the Kubelka–Munk equation the energy gap of the  $Ba_2YbSbO_6$  was determined to be  $3.62 \text{ eV}$ , which is relatively greater than that predicted by the band structure calculations. DFT calculations predict the  $Ba_2YbSbO_6$  perovskite behaving as a semiconductor with  $E_g=2.3 \text{ eV}$  while the diffuse reflectance results suggest a behavior of the material as a weak semiconductor with  $E_g=3.62 \text{ eV}$ . This difference occurs because in the DFT calculations, the exchange and correlation potential by Perdew, Burke and Ernzerhof [14] gives a very good approximation for the valence and conduction density of states, but is not very accurate for determining the energy gap in semiconductors due to self-interaction errors [21-22], for which it would be more interesting to use a potential specifically designed for this purpose, that uses local functional without Hartree-Fock exchange [23-24]. Thus, considering the uncertainty inherent in calculating the exact value of the Fermi level, from the results presented in figures 7b (DOS) and 8b (experimental energy gap), it is clear that the material behaves as a semiconductor. Our

experimental value of the band gap is comparable with that reported for oxygen-deficient SrTiO<sub>3</sub> ( $E_g=3.2$  eV) [25].

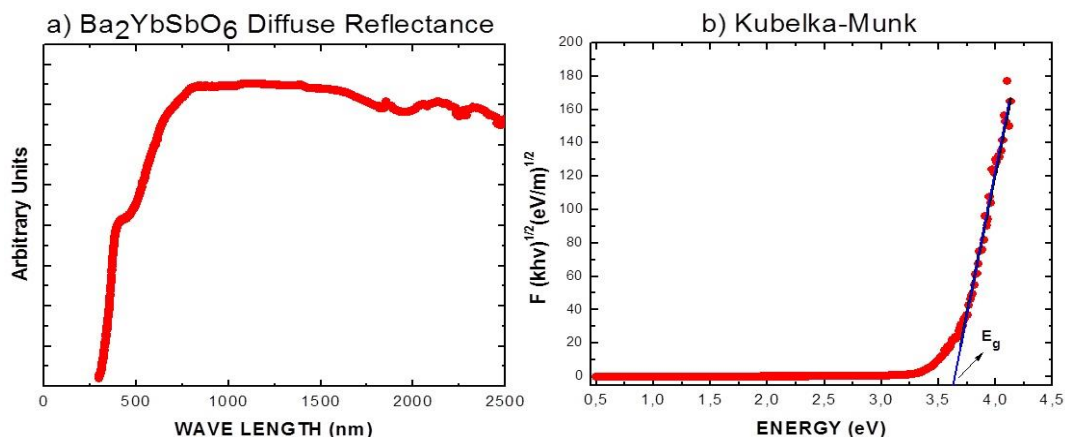


Figure. 8. (a) Diffuse reflectance results for the Ba<sub>2</sub>YbSbO<sub>6</sub> material. (b) Kubelka–Munk fitting.

In order to elucidate the dielectric characteristics of this compound, measurements of the dielectric constant as a function of frequency performed. The corresponding results are shown in Figure 9. As shown in the drawing, at low frequencies ( $\nu=100$  Hz) the value of the dielectric constant  $\epsilon=333$ , which is very close to the value reported for strontium titanate SrTiO<sub>3</sub> [26]. The value of the dielectric constant decreases dramatically with increasing frequency between 100 Hz and 300 Hz. Above  $\nu=400$  Hz, the dielectric constant decreases smoothly to the value  $\epsilon=14$  at  $\nu=10$  kHz. This result is consistent with reports, according to which, in semiconductor materials the value of the dielectric constant at low frequencies is maximum [27].

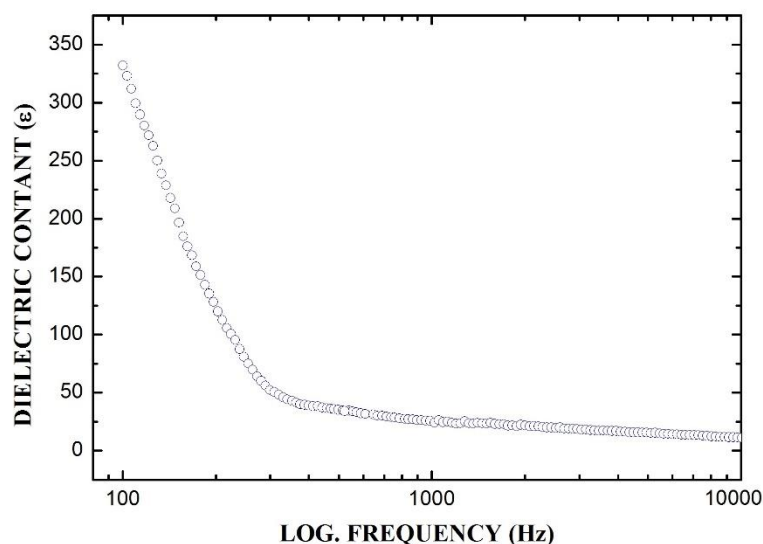


Figure. 9. Dielectric constant measured as a function of applied frequency for the Ba<sub>2</sub>YbSbO<sub>6</sub> complex perovskite.

In the *d-band* SrTiO<sub>3</sub>, the feature of large gap semiconductor is due to the broadening of the energy levels of the *Ti-O* octahedron and to the coexistence of free and delocalized excitations. In Ba<sub>2</sub>YbSbO<sub>6</sub> double perovskite there are two types of octahedrons, *Yb-O* and *Sb-O*, but it is clear in figures 6 and 7 that the delocalized states in the valence band are only due to the *d-Sb* orbitals. On the other hand, as observed in the inset of figure 1, there is a noticeable difference between the orientations of the *Yb-O*<sub>6</sub> and *Sb-O*<sub>6</sub> octahedral. This crystallographic feature can substantially modify the energy levels in the *Sb-O*<sub>6</sub> octahedra giving rise to a semiconductor behavior, which is dominant over the apparent conductor nature of the *Yb* spin-up valence electrons.

## 5. Conclusion

The synthesis of the Ba<sub>2</sub>YbSbO<sub>6</sub> new material by the solid-state reaction recipe was performed. Characterization of the crystalline structure through the X-ray diffraction technique and Rietveld refinement of the experimental data by using the GSAS code reveal this material crystallizes in a rhombohedral perovskite-like structure with cell parameter  $a=5.9104(1)$  Å and tilt angle  $\alpha=59.9993(0)^\circ$ . Measurements of diffuse reflectance permitted to determine the weak semiconductor character of this material with an energy gap of 3.62 eV. By means experiments of magnetic susceptibility as a function of temperature the paramagnetic response of the Ba<sub>2</sub>YbSbO<sub>6</sub> was analyzed. The fit to the Curie equation gives an effective magnetic moment of 4.31  $\mu_B$ , which is close to the expected value from the Hund's rules. The crystalline and band structures were calculated by using the Density Functional Theory. Structural results obtained by considering a rhombohedral perovskite belonging to the *R-3* space group are 98% in accordance with the experimental values. Close to the Fermi level, the band structure evidences strongly tendency to a half-metallicity behavior with semiconductor feature for the down spin orientation and conductor for the other. The mean value of the band gap is slightly smaller than the experimental value because the theoretical calculation was performed for the fundamental state,  $T=0$  K, while the experimental measurement was performed at room temperature. The theoretical effective magnetic moment calculated from DFT, which is majority due to the *Yb*<sup>3+</sup> isolated cation, is obtained to be 5.0  $\mu_B$ .

## Acknowledgements

This work was partially supported by Division of Investigations of the National University of Colombia.

## References

- [1] L.T. Corredor, J. Roa-Rojas, D.A. Landínez Téllez, R. Beltrán, P. Pureur, F. Mesquita and J. Albino Aguiar, J. Appl. Phys. **113** (2013) 17E302/1-3
- [2] D.P. Llamosa, D.A. Landínez Téllez and J. Roa-Rojas, Physica **B 404** (2009) 2726 (2009).
- [3] M. Baazaoui, S. Zemni, M. Boudard, H. Rahmouni, A. Gasmi, A. Selmi and M. Oumezzine, Int. J. Nanoelectronics and Materials. **3** (2010) 23
- [4] A.M. Glazer, Acta Crystallogr. **B 28** (1972) 3384

- [5] A.M. Glazer, Acta Crystallogr. **A 31** (1975) 756
- [6] P.M. Woodward, Acta Crystallogr. **B 53** (1997) 32
- [7] C.J. Howard, B.J. Kennedy and P.M. Woodward, Acta Crystallogr. **B 59** (2003) 463
- [8] M. Wakeshima, D. Harada and Y. Hinatsu, J. Alloys and Compd. **287** (1999) 130
- [9] M. Wakeshima, D. Harada, Y. Hinatsu and N. Masaki, J. Solid State Chem. **47** (1999) 618
- [10] M. Wakeshima, D. Harada and Y. Hinatsu, J. Mater. Chem. **10** (2000) 419
- [11] C.M. Bonilla, D.A. Landínez Téllez, J. Arbey Rodríguez, E. Vera López and J. Roa-Rojas, Phys. **B 398** (2008) 208
- [12] A.C. Larson and R.B. von Dreele, General Structure Analysis System GSAS (Los Alamos National Laboratory Report LAUR 2000), pp. 86-748.
- [13] P. Blaha, K. Schwarz, G.K.H. Madsen, D. Kvasnicka and J. Luitz, WIEN2k, an Augmented Plane Wave + Local Orbitals Program for Calculating Crystal Properties (Techn. Universität Wien, Vienna, 2001) ISBN 3-9501031-1-2.
- [14] S. Kausar, S. Joshi and A. Srivastava, Int. J. Nanoelectronics and Materials. **7** (2014) 77
- [15] F. D. Murnaghan, Proc. Natl. Acad. Sci. USA **30** (1944) 244
- [16] M.W. Lufaso and P.M. Woodward, Acta Crystallogr. **B 57** (2001) 725
- [17] W. Wondratschek, *International Tables for Crystallography* (2006), Vol. A, Chapter 8.3, pp. 732-740.
- [18] E. Parthé, L. Gelato, B. Chabot, M. Penzo, K. Cenxual, R. Gladyshevskii, TYPIX Standardized and crystal chemical characterization of inorganic structure types. In: Gmelein Handbook of Inorganic and Organometallic Chemistry, 8th ed. (Springer, Berlin, 1993).
- [19] C. Kittel, *Introduction to Solid State Physics*, 6th Ed., John Wiley & Sons, Inc., New York, (1997) pp. 482
- [20] M. Bonilla, D.A. Landínez Téllez, J.A. Rodríguez, J. Albino Aguiar and J. Roa-Rojas, J. of Magn. Mater. **320** (2008) e397
- [21] H. Einollahzadeh, R.S. Dariani and S.M. Fazeli, Solid State Commun. **229** (2016) 1
- [22] Y. Zhao and D. G. Truhlar, J. of Chem. Phys. **130** (2009) 074103/1-3
- [23] T. Higuchi, T. Tsukamoto, N. Sata, M. Ishigame, Y. Tezuka and S. Shin, Phys. Rev. **B 57** (1998) 6978
- [24] N. Kulagin, J. Dojcilovic and D. Popovic, Cryogenics **41** (2001) 745
- [25] Y. Zhao and D. G. Truhlar, J. Chem. Phys. **125** (2006) 194101/1-18
- [26] Y. Zhao and D. G. Truhlar, Acc. Chem. Res. **41** (2008) 157
- [27] E. Hosseine, Int. J. Nanoelectronics and Materials **8** (2015) 91



## **AUTHOR GUIDELINES FOR JOURNAL ARTICLE**

### **Introduction**

This document enables the user to have a better understanding of rules and regulations used for writing journals. However, each institute has its own template so it is advised that after writing any journal or publication, refer to your specific institute references for writing journals and publications.

### **Format**

All files should be submitted as a Microsoft Word Document.

### **Article Length**

Articles should usually be between **4000 and 10000 words** in length. This includes all text including references and appendices. Please allow roughly **280 words** for each figure or table.

### **Article Title**

A title of not more than **16 words** is advised.

### **Article Title Page**

An Article Title Page should be submitted alongside each individual article using the template provided.

This should include:

- Article Title
- Author Details (see below)
- Acknowledgements
- Author Biographies
- Structured Abstract (see below)
- Keywords (see below)
- Article Classification (see below)

### **Author Details**

Details should be supplied on the Article Title Page including:

- Full name of each author
- Affiliation of each author, at time research was completed
- Where more than one author has contributed to the article, details of who should be contacted for correspondence
- E-mail address of the corresponding author

### **Structured Abstract**

Authors should supply a structured abstract on the Article Title Page, set out under 4-7 sub-headings:

- Purpose (mandatory)
- Design/methodology/approach (mandatory)

- Findings (mandatory)
- Research limitations/implications (if applicable)
- Practical implications (if applicable)
- Social implications (if applicable)
- Originality/value (mandatory)

Maximum should roughly be **250** words in total (including keywords and article classification).

### **Keywords**

You should provide up to **10 keywords** on the Article Title Page, which encapsulate the principal topics of the paper.

### **Article Classification**

Categorize your paper on the Article Title Page, under one of these classifications:

- Research paper
- Viewpoint
- Technical paper
- Conceptual paper
- Case study
- Literature review
- General review.

### **Headings**

Headings should be concise, with a clear indication of the distinction between the hierarchies of headings.

The preferred format is for first level headings to be presented in bold format and subsequent sub-headings to be presented in medium italics.

### **Notes/Endnotes**

Notes or Endnotes should be used only if absolutely necessary and must be identified in the text by consecutive numbers, enclosed in square brackets and listed at the end of the article.

### **Research Funding**

Authors must declare all sources of external research funding in their article and a statement to this effect should appear in the Acknowledgements section. Authors should describe the role of the funder or financial sponsor in the entire research process, from study design to submission.

## Figures

All Figures (charts, diagrams, line drawings, web pages/screenshots, and photographic images) should be submitted in electronic form.

All Figures should be of high quality, legible and numbered consecutively Graphics may be supplied in color to facilitate their appearance on the online database.

□ Figures created in Microsoft Word, Microsoft PowerPoint, Microsoft Excel and Illustrator should be supplied in their native formats. Electronic figures created in other applications should be copied from the origination software and pasted into a blank Microsoft Word document or saved and imported into an Microsoft Word document or alternatively create a .pdf file from the origination software.

□ Figures which cannot be supplied in as the above are acceptable in the standard image formats which are: .pdf, .ai, and .eps. If you are unable to supply graphics in these formats then please ensure they are .tif, .jpeg, or .bmp at a resolution of at least 300dpi and at least 10cm wide.

□ To prepare web pages/screenshots simultaneously press the "Alt" and "Print screen" keys on the keyboard, open a blank Microsoft Word document and simultaneously press "Ctrl" and "V" to paste the image. (Capture all the contents/windows on the computer screen to paste into Microsoft Word, by simultaneously pressing "Ctrl" and "Print screen".)

Photographic images should be submitted electronically and of high quality. They should be saved as .tif or .jpeg files at a resolution of at least 300dpi and at least 10cm wide. Digital camera settings should be set at the highest resolution/quality possible.

## Tables

Tables should be typed and included in a separate file to the main body of the article. The position of each table should be clearly labelled in the body text of article with corresponding labels being clearly shown in the separate file.

Ensure that any superscripts or asterisks are shown next to the relevant items and have corresponding explanations displayed as footnotes to the table, figure or plate.

## References

References to other publications must be in Harvard style and carefully checked for completeness, accuracy and consistency. This is very important in an electronic environment because it enables your readers to exploit the Reference Linking facility on the database and link back to the works you have cited through CrossRef.

You should cite publications in the text, for example: (Adams, 2006) using the first named author's name or (Adams and Brown, 2006) citing either names of two, or (Adams et al., 2006), when there are three or more authors. At the end of the paper a reference list in alphabetical order should be supplied:

### **References for Books**

For books you should follow below template:

Surname, Initials (year), Title of Book, Publisher, Place of publication.

### **References for Book Chapters**

For book chapters you should follow below template:

Surname, Initials (year), "Chapter title", Editor's Surname, Initials, Title of Book, Publisher, Place of publication, pages.

*e.g.* Calabrese, F.A. (2005), "The early pathways: theory to practice – a continuum", in Stankosky, M. (Ed.), *Creating the Discipline of Knowledge Management*, Elsevier, New York, NY, pp. 15-20

### **References for Journals**

For journals you should follow below template:

Surname, Initials (year), "Title of article", Journal Name, volume, number, pages.

*e.g.* Capizzi, M.T. and Ferguson, R. (2005), "Loyalty trends for the twenty-first century", *Journal of Consumer Marketing*, Vol. 22 No. 2, pp. 72-80.

### **References for Published Conference Proceedings**

For journals you should follow below template:

Surname, Initials (year of publication), "Title of paper", in Surname, Initials (Ed.), Title of published proceeding which may include place and date(s) held, Publisher, Place of publication, Page numbers.

*e.g.* Jakkilinki, R., Georgievski, M. and Sharda, N. (2007), "Connecting destinations with an ontology-based e-tourism planner", in *Information and communication technologies in tourism 2007 proceedings of the international conference in Ljubljana, Slovenia, 2007*, Springer-Verlag, Vienna, pp. 12-32.

### **References for Unpublished Conference Proceedings**

For unpublished conference proceedings you should follow below template:

Surname, Initials (year), "Title of paper", paper presented at Name of Conference, date of conference, place of conference, available at: URL if freely available on the internet (accessed date).

*e.g.* Aumueller, D. (2005), "Semantic authoring and retrieval within a wiki", paper presented at the European Semantic Web Conference (ESWC), 29 May-1 June, Heraklion, Crete, available at:<http://dbs.uni-leipzig.de/file/aumueller05wiksar.pdf> (accessed 20 February 2007).

### **References for Working Papers**

For Working Papers you should follow below template:

*Surname, Initials (year), "Title of article", working paper [number if available], Institution or organization, Place of organization, date.*

*e.g. Moizer, P. (2003), "How published academic research can inform policy decisions: the case of mandatory rotation of audit appointments", working paper, Leeds University Business School, University of Leeds, Leeds, 28 March.*

### **References for Encyclopedia Entries (no author or editor)**

For encyclopedia entries you should follow below template:

*Title of Encyclopedia (year) "Title of entry", volume, edition, Title of Encyclopedia, Publisher, Place of publication, pages.*

*e.g. Encyclopaedia Britannica (1926) "Psychology of culture contact", Vol. 1, 13th ed., Encyclopaedia Britannica, London and New York, NY, pp. 765-71.*

### **References for Newspaper Articles (non-authored)**

For Newspaper Articles you should follow below template:

*Newspaper (year), "Article title", date, pages.*

*e.g. Daily News (2008), "Small change", 2 February, p. 7.*

### **References for Electronic Sources**

If it is available online, the full URL should be supplied at the end of the reference, as well as a date that the resource was accessed.

*e.g. Castle, B. (2005), "Introduction to web services for remote portlets", available at: <http://www-128.ibm.com/developerworks/library/ws-wsrp/> (accessed 12 November 2007).*

Standalone URLs, i.e. without an author or date, should be included either within parentheses within the main text, or preferably set as a note (Roman numeral within square brackets within text followed by the full URL address at the end of the paper).

=====

For more information

#### **Contact us:**

The Scientific Institute for Advanced Training and Studies

Email: [publisher@siays.co.uk](mailto:publisher@siays.co.uk)

Phone: (0060) 11 113 331 80

WhatsApp & viber

Facebook: <https://www.facebook.com/siats.mutamd?ref=bookmarks>

Experimental and Theoretical NANOTECHNOLOGY

<http://etn.siats.co.uk>

Guidelines link: <http://www.siats.co.uk/author-guidelines-for-journal-article/>

## **Content**

1. COMPARATIVE STUDY OF ATTENUATION PROPERTIES OF SOME TERNARY BORATE GLASS SYSTEMS.....123
2. MODELLING OF SILICON BASED ELECTROSTATIC ENERGY HARVESTER FOR CARDIAC IMPLANTS.....129
3. NUMERICAL INVESTIGATION OF NATURAL CONVECTION HEAT TRANSFER IN A CAVITY UTILIZING AL<sub>2</sub>O<sub>3</sub>-WATER NANOFLUID: EFFECT OF BAFFLE HEIGHT.....137
4. SINGLE WALLED CARBON NANOTUBES REINFORCED INTERMETALLIC TINI MATRIX NANOCOMPOSITES BY SPARK PLASMA SINTERING.....145
5. STRUCTURAL, MAGNETIC, ELECTRIC AND ELECTRONIC ASPECTS OF THE BA<sub>2</sub>YBSBO<sub>6</sub> PEROVSKITE MATERIAL..... 153